bioRxiv preprint doi: https://doi.org/10.1101/481887; this version posted June 12, 2019. The copyright holder for this preprint (which was not certified by peer review) is the author/funder. All rights reserved. No reuse allowed without permission.

A synthetic morphogenic membrane system that responds with self-organized shape changes to local light cues

Konstantin Gavriljuk[1,3], Bruno Scocozza[1,3], Farid Ghasemalizadeh[1,3], Akhilesh P. Nandan[1], Manuel Campos Medina[1], Hans Seidel[1], Malte Schmick[1], Aneta Koseska[1,2], Philippe I. H. Bastiaens[1,2,4,*]

Affiliations

[1]Department of Systemic Cell Biology, Max Planck Institute for Molecular Physiology, 44227 Dortmund, Germany

[2]Faculty of Chemistry and Chemical Biology, TU Dortmund, 44227 Dortmund, Germany

[3]These authors contributed equally

[4]Lead Contact

*Correspondence: philippe.bastiaens@mpi-dortmund.mpg.de (P.B.)

SUMMARY

Cytoskeletal dynamics regulated by extracellular signaling provides the morphogenic plasticity of eukaryotic cells. To uncover fundamental principles of cell morphogenesis, we reconstituted an out-of-equilibrium Synthetic Morphogenic Membrane System (SynMMS) consisting of a dynamic microtubule (MT)-aster together with a light-triggered signaling system in cell sized vesicles. Signaling is actuated by light-stimulus induced translocation of AuroraB kinase to the membrane that phosphorylates the microtubule regulator stathmin. We found that in the presence of soluble phosphatase activity, a membrane proximal tubulin gradient is generated that locally promotes growth of MT filaments. The resulting membrane deformations enable recursive interactions of astral MTs with the signaling system, creating global self-organized morphological states that can transform upon local light irradiation. This interdependence that necessarily occurs in mammalian cells with a deformable membrane thereby enables both morphological plasticity as well as shape stabilization to extracellular signals in dependence on prior morphology.

Keywords

Synthetic proto-cell, cell morphogenesis, reconstituted microtubule and signaling system, dimensionality reduction, signaling gradient, membrane-cytoskeletal interactions, interdependence of signaling and cytoskeleton, morphological plasticity, self-organization

bioRxiv preprint doi: https://doi.org/10.1101/481887; this version posted June 12, 2019. The copyright holder for this preprint (which was not certified by peer review) is the author/funder. All rights reserved. No reuse allowed without permission.

INTRODUCTION

Mammalian cells acquire their shape which is tightly linked to their biological function by dynamic cytoskeletal systems that deform the plasma membrane. Cell shape changes and motility are driven by the microtubule (MT) and actin filament systems, which operate at different length- and time-scales (Huber et al., 2015). Actin filaments dictate the rapid, more local morphological dynamics at the cell periphery, whereas MTs are far more long lived, persist over longer distances and are globally organized through MT organizing centers (MTOC) during developmental processes. This enables them to function as a single cohesive network on the scale of the cell that not only operates as a compass for front-back polarity in cell movement, but also generates and maintains global cell shapes during differentiation (Etienne-Manneville, 2004, 2013; Muroyama and Lechler, 2017; Vignaud et al., 2012).

Cells reorganize their MT-supported shape upon exposure to extracellular morphogen signals that interact with receptors on their surface. This morphological response originates from morphogen-triggered action of Rho GTPases on microtubules through regulation of microtubule-associated proteins (MAPs) such as stathmin. Stathmin in turn affects microtubule dynamics by modulating the cytoplasmic pool of free tubulin through sequestration of tubulin dimers (Curmi et al., 1997). However, directed MT-growth towards a local morphogen source further requires spatially constraining both the signaling, as well as the activity of these freely diffusible MAPs.

Rho GTPase mediated signaling itself is actuated and locally confined via the universal mechanism of dimensionality reduction (Adam and Delbrück, 1968; Oancea and Meyer, 1998; Shen and Meyer, 1999). This occurs by the drastic increase in local enzyme concentration and thereby signaling activity upon translocation of, for example, Pak1 kinase to activated Rac1/Cdc42 on the plasma membrane (Daub et al., 2001; Leung et al., 1995; Manser et al., 1994). This spatial confinement of the kinase activity leads to local phosphorylation of the diffusible MAP stathmin, thereby generating gradients of phosphorylated stathmin that cannot bind tubulin (Niethammer et al., 2004). However, it is unclear how local release of tubulin from phosphorylated stathmin, which can freely diffuse in the cytoplasm, guides MT-growth in the direction of extracellular cues. Even more, to ensure a global polarizing morphological response, the whole MT-network needs to be reorganized and stabilized in the direction of an extracellular stimulus. One mechanism to achieve stabilization of the MT-supported shapes is the local feedback amplification of signaling that initially triggered the growth of MTs (Wu and Bezanilla, 2018). Indeed, MTs do not only contribute to morphogenesis by their mechanical or transport capabilities, but also enhance their own growth via activation of Rho mediated signaling (Etienne-Manneville, 2013; Etienne-Manneville and Hall, 2002; Waterman-Storer et al., 1999; Wittmann et al., 2003). How this recursive coupling between MT-growth and signaling is realized on the molecular level is still unclear and the question how cell shapes emerge from this bi-directional interaction has not been addressed.

Reconstituted systems have revealed much about the fundamental mechanisms of self-organized cell polarity that can arise from the interplay of the MT-cytoskeleton and motor proteins (Baumann and Surrey, 2014; Juniper et al., 2018; Laan et al., 2012; Letort et al., 2016; Nédélec et al., 1997; Pinot et al., 2009; Surrey et al., 2001). Herein, we follow a similar bottom-up approach to elucidate how the interdependence between the dynamic MT-cytoskeleton and signaling at the membrane affects cellular morphogenesis. For this, we generated a minimal synthetic system in a cell-sized liposome, consisting of centrally organized MT-cytoskeleton and a light-induced signaling pathway that affects MT-growth. To mimic the canonical Rac1-Pak1 pathway, we introduced the iLID/SspB optical dimerizer system (Guntas et al., 2015) into giant unilamellar vesicles (GUVs). With this system, AuroraB kinase can be translocated to the membrane and locally activated in response to blue light. This triggers membrane proximal stathmin phosphorylation that combined with ubiquitous dephosphorylating activity creates a stathmin phosphorylation gradient. This signaling system responds to localized light cues in

bioRxiv preprint doi: https://doi.org/10.1101/481887; this version posted June 12, 2019. The copyright holder for this preprint (which was not certified by peer review) is the author/funder. All rights reserved. No reuse allowed without permission.

analogy to morphogen responding signaling systems in cells. Importantly, we demonstrate that the gradient generating phosphorylation/dephosphorylation cycle near the membrane promotes local MT-polymerization by generating an elevated membrane proximal concentration of free tubulin. Our findings demonstrate that the resulting membrane deformations do not only define the cell shape, but also constitute a local reaction medium through which the MT-cytoskeleton and signaling can recursively interact without necessitating direct biochemical feedback. This membrane-mediated recursion together with global depletion of free MTs and AuroraB leads to self-organized shapes that can be transformed and stabilized upon extracellular cues. A minimal theoretical framework of the self-amplifying interactions between the cytoskeletal and signaling systems, individually undergoing substrate depletion dynamics, captured the initial morphological states as well as light-induced morphological transitions. We thereby show that the interdependence of MT dynamics and signaling as mediated by the deformable membrane is a fundamental mechanism by which cells reorganize their shape in response to extracellular signals.

RESULTS

MT-asters that deform the membrane self-organize into a polar protrusion morphology

To investigate which morphologies emerge from the collective behavior of centrally organized dynamic MTs that interact via a deformable membrane, we encapsulated purified centrosomes together with tubulin and GTP in GUVs using cDICE (Abkarian et al., 2011) (STAR Methods). This generated dynamically instable (Mitchison and Kirschner, 1984) MT-asters with different sizes inside GUVs, as determined by the encapsulated tubulin concentration (Figures S1A – S1C). The deformability of the membrane was controlled by the outside osmolarity. The GUVs containing the self-assembled MT-asters were monitored by confocal laser scanning microscopy (CLSM) using trace amounts of fluorescently labeled tubulin (~10 % Alexa568- or Alexa488-tubulin, STAR Methods). Encapsulating low tubulin concentrations (15 – 25 μM) under isosmotic conditions resulted in GUVs with a spherical morphology and centrally positioned asters whose size was smaller than that of the GUV (Figures 1A and 1B). Higher tubulin concentrations (35 – 40 μM) under the same osmotic pressure resulted in cortical MTs with peripheral centrosome positioning, as previously observed for MT-asters from *X. laevis* egg extracts growing inside a rigid boundary (Pinot et al., 2009) (Figures 1A and 1B). However, decreasing the membrane tension by increasing outside osmolarity led to a polar morphology with one or more protrusions, reflected both in peripheral centrosome positioning as well as increased GUV eccentricity (Figures 1A and 1B). Importantly, we found that these morphologies were dynamically maintained, since upon increase of the outside osmolarity, the dynamic MT-asters could remodel the membrane and displayed a morphological transition from spherical GUVs with cortical MTs to polar GUVs with one or more protrusions (Figure 1C). Further increase of outside osmolarity did not affect the shape of the GUVs (Figure S1D), suggesting that the system with a large aster and a deformable membrane always converges to this polar morphology.

The convergence of many bending MTs into these polar protrusions indicates that they were initially created by small membrane deformations that served as a capture-site for neighboring microtubules. This self-induced capture occurs because of the decreased catastrophe frequency of MTs contacting the membrane at shallow angle near the protrusion, which results in gliding towards the protrusion center (Faivre-Moskalenko and Dogterom, 2002; Janson et al., 2003; Soheilypour et al., 2015). We therefore refer to these membrane deformations containing MT-bundles as self-induced capture (SIC) protrusions (Figure 1D).

bioRxiv preprint doi: https://doi.org/10.1101/481887; this version posted June 12, 2019. The copyright holder for this preprint (which was not certified by peer review) is the author/funder. All rights reserved. No reuse allowed without permission.

To study whether and which morphological transitions can be induced by increasing aster size, the growth of small encapsulated asters was promoted by raising the temperature from 20 °C to 34 °C in GUVs with either a rigid or deformable membrane. This is equivalent to a morphogen signal that globally affects MT-aster size. Upon raising the temperature in GUVs with high membrane tension, MT growth led to centrosome decentering, resulting in the formation of semi-asters (Figure 1E; Figures S1E and S1F; Video S1). This MT-aster organization minimizes the filament elastic energy within the rigid GUVs constrains, as previously described (Pinot et al., 2009). However, in GUVs with a deformable membrane, temperature-induced growth of MTs evolved the system from a morphology with isotropically distributed SIC protrusions to a stable polar protrusion morphology. During this process, the centrosome was decentered while the transient SIC protrusions converged to a single one at the opposite pole (Figures 1F and 1G; Video S2). This indicated that growing MT-bundles in SIC protrusions provided an initially random directional push to the centrosome which polarized the GUV by a recursive process of SIC protrusion coalescence and centrosome decentering. This was even more apparent in a GUV with higher membrane deformability, where this recursive process generated a bipolar morphology with one SIC protrusion near the centrosome and one at the opposite pole (Figure 1G). Thus, the physical coupling between the astral MTs at the level of the deformable membrane gave rise to collective MT behavior resulting in a symmetry broken morphology with protrusions at opposite poles. To next investigate if and how morphological transitions can be induced by extracellular signals that affect MT growth, we reconstituted a light-responsive signaling system that biochemically affects aster size.

The light-induced signaling system generates a membrane proximal tubulin gradient

In cells, extracellular morphogen information is transmitted by cell surface receptors leading to the recruitment of Pak1 kinase to activated GTPases that phosphorylates the MT-regulator stathmin (Daub et al., 2001), thereby decreasing its affinity for tubulin. The resulting higher free tubulin concentration in the cytoplasm affects MT-cytoskeletal growth (Figure 2A, left), setting the causal basis for signaling-induced morphological transitions. To capture these principles of dimensionality reduction-actuated signaling, we encapsulated the iLID/SspB optical dimerizer system (Guntas et al., 2015) to translocate the stathmin phosphorylating AuroraB kinase (Gadea and Ruderman, 2006) to the membrane. We used AuroraB for this purpose because it shares the same substrate –stathmin– as Pak1, albeit in the different physiological context of mitosis (Wang et al., 2011), but displays higher in vitro activity. AuroraB was fused to SspB (SspB-AuroraB) and iLID associated with the membrane via a C2 phosphatidylserine-binding domain (C2-iLID) (Figure 2A, right). SspB-AuroraB contained the $INCENP_{in\text{-}box}$ (Inner centromere protein A, amino acids 834 – 902) peptide, enabling AuroraB activation by trans-phosphorylation (Sessa et al., 2005; Zaytsev et al., 2016). SspB-AuroraB was fluorescently labeled with Alexa-488, and the amount of translocation could be controlled by blue light intensity (Figure 2B). Residual binding to C2-iLID in the absence of photo-activating light determined basal SspB-AuroraB activity, whereas saturatable binding to C2-iLID limited the maximal achievable activity on the membrane. Interestingly, we observed that SspB-AuroraB clusters were formed on the membrane upon its translocation, irrespective of ATP and therefore kinase activity (Figure 2C; Figure S2E). Clustering is a specific property of AuroraB and not of the iLID/SspB proteins, since it did not occur for a SspB-λ-phosphatase fusion construct (SspB-PPλ). The observed distribution of Aurora clusters was not random but exhibited spatial order (Figure 2D). Quantification of the spatial SspB-AuroraB pattern recurrences on the membrane by means of information entropy ((Marwan et al., 2007a), STAR Methods) revealed that the spatial order increased for higher SspB-AuroraB depletion from the lumen (Figure 2D). In contrast, the spatial SspB-PPλ distribution displayed overall low information entropy values, independent of the fraction of depleted molecules from the lumen.

bioRxiv preprint doi: https://doi.org/10.1101/481887; this version posted June 12, 2019. The copyright holder for this preprint (which was not certified by peer review) is the author/funder. All rights reserved. No reuse allowed without permission.

This indicates that light-induced translocation drives self-organized SspB-AuroraB pattern formation based on substrate-depletion (Figure 2E).

To next investigate how the system responds to a local light stimulus, a region of the GUV was continuously irradiated with blue light. Maximal SspB-AuroraB translocation was observed in the irradiated area, whereas the dissociation kinetics in the areas that were not photo-activated (Figure 2F lower panel; Figures S2A – S2C) was sufficiently fast in comparison to its diffusion along the membrane to generate a declining gradient of translocated SspB-AuroraB from this area (Figure 2F upper panel; Figure S2D). Local light irradiation thereby mimics the spatially graded translocation response of AuroraB as if originating from an extracellular morphogen gradient.

To establish how AuroraB kinase activity on the membrane regulates MT-aster dynamics via stathmin, we first quantified the effects of stathmin on MT dynamics by single filament TIRF assays (STAR Methods). Increase in stathmin concentration linearly decreased MT-growth speed and abruptly increased catastrophe frequency (Figure S3A), whereas phosphorylated stathmin (pStathmin) only weakly affected MT-dynamics (Figure S3B). Interaction of fluorescently tagged stathmin with MT plus ends was not observed, concluding that stathmin affects MT-dynamics purely through sequestering free tubulin (Curmi et al., 1997; Howell et al., 1999; Niethammer et al., 2004). Stathmin, in contrast to pStathmin, therefore also reduced MT-aster size (Figures 3A) and thereby affected GUV morphology (Figure 3B). Encapsulating high tubulin concentrations (40 µM) with 5 µM stathmin resulted in small asters leading to a spherical morphology, whereas co-encapsulation of 5 µM pStathmin resulted in the previously observed polar morphology with high tubulin (Figure 1A). These results show that MT-dynamics can be biochemically coupled to a kinase-based signaling system that affects the availability of free tubulin via stathmin phosphorylation.

In cells, soluble kinase and phosphatase activity give rise to a steady state fraction of phosphorylated stathmin in the cytoplasm, before a signal-induced recruitment of the kinase to the membrane changes this kinetic balance. We therefore first measured bulk solution kinetics of stathmin phosphorylation by SspB-AuroraB and dephosphorylation by PPλ (Table 1) using an organic dye-containing variant of the stathmin phosphorylation FRET sensor COPY (Niethammer et al., 2004) (Atto532-stathmin-Atto655: COPY^{o} (organic)) (Figures S4A and S4B). Ratiometric quantification of the phosphorylation of COPY^{o} after sequential addition of SspB-Aurora and PPλ in solution demonstrated that SspB-AuroraB/PPλ-mediated phosphorylation/dephosphorylation cycle maintains a steady-state pStathmin level in the presence of ATP (Figure 3C; Figure S5A). The kinetics derived in this manner (Figure S4C; Table 1) showed that before kinase translocation, stathmin is maintained at a low phosphorylation level in the lumen of the GUV, when the concentrations of SspB-AuroraB and PPλ are equal (1 µM). This low phosphorylation of stathmin results in a high level of tubulin sequestration and therefore less available tubulin for MT polymerization.

To explore how the stathmin phosphorylation cycle is spatially affected by kinase translocation and how this affects tubulin concentration, we first simulated the reactions between tubulin and stathmin as mediated by SspB-Aurora and PPλ with a reaction-diffusion model using measured enzymatic and association/dissociation parameters (Figures S4C and S4D; Table 1; STAR Methods). The simulations revealed that recruiting kinase activity to the membrane re-balances the phosphorylation cycles' steady states. Decreasing SspB-AuroraB concentration in solution further suppresses general phosphorylation of stathmin, while increased kinase activity at the membrane can locally overcome PPλ thereby constituting a source of pStathmin. Diffusion of pStathmin away from this source yields a gradient emanating from the membrane that is maintained by a chemical energy driven net-flux of stathmin-tubulin complex towards high kinase concentration. Importantly, the simulations also revealed that the

bioRxiv preprint doi: https://doi.org/10.1101/481887; this version posted June 12, 2019. The copyright holder for this preprint (which was not certified by peer review) is the author/funder. All rights reserved. No reuse allowed without permission.

phosphorylation/dephosphoryaltion cycle also generates a gradient of free tubulin that coincides with the pStathmin gradient (Figure 3D; Figures S4E and S4F). In other words, the stathmin phosphorylation cycle at the membrane constitutes an ATP-driven tubulin 'pump' (Figure 3E) that, due to the rapid kinetics of tubulin release from phosphorylated stathmin, can maintain an out-of-equilibrium concentration of tubulin near the membrane.

In order to now measure and characterize the predicted pStathmin gradient in a biochemically open system, we first introduced COPY^{o} to the outside of GUVs that were functionalized with iLID (STAR Methods). Ratiometric FRET measurement of COPY^{o} showed that steep (~0.5 µm) gradients emanated outward from the GUV membrane upon light-induced recruitment of SspB-AuroraB only in the presence of PPλ (Figures 3F and 3G). This allowed to estimate optimal SspB-AuroraB and PPλ concentrations for the pStathmin gradient inside GUVs. Upon encapsulation of the full signaling system, COPY^{o} was maintained in a dephosphorylated steady-state in the lumen, whereas light-induced translocation of SspB-AuroraB resulted in clear gradients from the GUV membrane (Figures 3H and 3I; Figures S5B – S5E). Strikingly, these gradients mainly emanated from patterned structures, most likely originating from the spatially organized clusters of active SspB-AuroraB.

To test if this light-induced membrane proximal tubulin gradient affects MT growth, we encapsulated the full signaling system together with the cytoskeletal module in GUVs with a rigid membrane. We will further refer to the encapsulated signaling system together with the cytoskeletal module as a Synthetic Morphogenic Membrane System (SynMMS). Light-induced SspB-AuroraB translocation resulted in centrosome decentering due to MT-growth (Figures 3J – 3L; Video S3), similarly to the temperature-induced MT-growth in a rigid GUV (Figure 1E). Strikingly, the centrosome reverted to a central positioning within the GUV upon light removal, indicating that this process was reversible (Figure 3L). This firmly established MT-growth activation by the reconstituted tubulin gradient-generating signaling system, and thereby allows to investigate how signaling induces morphological transitions in a system with a deformable membrane.

The deformable membrane establishes recursive interactions between signaling and astral MTs

In order to investigate if MT-induced membrane deformation can be brought about by activating the signaling system, we globally irradiated a spherical SynMMS with a small aster under hypertonic conditions. This led to SspB-AuroraB translocation, upon which membrane protrusions were generated (Figures 4A and 4B; Video S4). These isotropically distributed protrusions were small, curved back on the GUV and were stable for a prolonged period of time (Figure 4C left kymograph). Although the condition in which small asters are formed resulted in a high fluorescence background from soluble tubulin, MTs connecting the aster to the protrusions could be observed as well as in other activated SynMMS (Figure 4A; Figure S6A). The connection between the aster and the protrusions was additionally apparent from the coupled dynamics of centrosome positioning and protrusion genesis (Figure 4C left kymograph). These bending protrusions thus likely originated from dynamically instable MTs, whose growth was accelerated once their plus ends encountered the enhanced tubulin concentration proximal to the membrane. This was different from the light-induced response in SynMMS lacking centrosomes, where enhanced MT-growth led to increased bundling of cortical MTs (Figure S7). Although a tangential protrusion could be generated by the growing cortical MTs (Figure S7A, right), no isotropically distributed protrusions were generated due to the lack of a centrosome.

We confirmed that stathmin is essential to couple the signaling system to MT-dynamics by examining the response of a SynMMS with a small aster that lacked stathmin (SynMMS$^{\text{-stat}}$)

bioRxiv preprint doi: https://doi.org/10.1101/481887; this version posted June 12, 2019. The copyright holder for this preprint (which was not certified by peer review) is the author/funder. All rights reserved. No reuse allowed without permission.

(Figures 4D – 4F; Video S4). This SynMMS^{-stat} did not generate protrusions upon blue light induced SspB-AuroraB translocation and its centrosome fluctuated around the central position due to the transient interaction of the dynamically instable astral MTs with the membrane. However, we observed rapid fluctuations in the intensity of SspB-AuroraB on the membrane in SynMMS^{-stat}. This indicated that the transient interaction of the astral MTs with the membrane locally enhanced the concentration of SspB-AuroraB. We also observed that SspB-AuroraB was highly enriched in the protrusions after light-activation of SynMMS (Figures 4A lower panel and 4C right kymograph). To investigate if this amplification of signaling is due to membrane deformation, we induced the translocation of SspB-AuroraB in a SynMMS^{-stat} with large asters and polar morphology. Light-induced translocation enhanced the density of SspB-AuroraB in both polar as well as in transient off-axis protrusions, which were not observed for the encapsulated C2-iLID/SspB-AuroraB system alone (Figures 4G and 4H; Figure S8). This shows that SspB-AuroraB is preferentially recruited to MT-induced deformed membrane surfaces, likely caused by increased ratio of membrane surface to lumen volume in concave membrane deformations (Rangamani et al., 2013). Furthermore, reaction-diffusion simulations showed that MT-induced membrane protrusions not only recruit more SspB-AuroraB, but also have a stronger tubulin gradient (Figure S6B). The deformable membrane therefore necessarily establishes feedback interactions between the signaling and the cytoskeletal systems, where MT-induced deformation enhances signaling, which in its turn promotes MT growth and thereby membrane deformation.

We speculated that this positive feedback could confer stability to the generated protrusions even after removal of the stimuli and thereby generate a morphological memory in the direction of the stimulus. To experimentally test this idea, we transiently irradiated in sequence several areas of a SynMMS that had an MT-aster supported oval shape and peripheral centrosome positioning. Irradiation in the right area immediately triggered the formation of a MT-induced protrusion that persisted after switching the irradiated area to the other side and evolved into a long protrusion (Figures 4I and 4J; Video S5). Subsequent irradiation on the opposite side of this SynMMS also induced the formation of persistent protrusions that remained after switching the irradiated area to the lower part of the SynMMS. In this third area, no protrusions were formed, indicating that MTs were depleted by the protrusions formed in the previously irradiated areas. In contrast, a morphologically similar control SynMMS^{-stat} did not form stabilized protrusions in any of the sequentially irradiated areas (Figure S6C). The persistence of the protrusions formed as a response to the transient light-cues thus demonstrated that they can be stabilized due to the recursive interactions at the membrane, enabling a morphological response that is dependent on previous stimuli.

A paradigmatic reaction-diffusion model captures dynamical features of SynMMS

Since the previous experiments demonstrate that SynMMS exhibits a morphological memory to previous stimuli, it naturally follows that its response should depend on its initial morphology. Hence, we quantified the shapes of SynMMS and compared these to the encapsulated cytoskeletal system alone (Figure 5A). Three coarse-grained morphological classes, spherical (semi-asters), polar, and star-like, were identified using jointly two morphometric classification parameters (Figure S6E, STAR Methods). For the encapsulated cytoskeletal system alone, spherical and polar morphologies comprised the majority of shapes (consistent with Figure 1), whereas for SynMMS, an additional star-like morphology with SIC protrusions was observed.

Understanding how these morphologies arise and how plastic they are in their ability to respond to light stimuli, requires a formal description of how dynamic morphological behavior emerges from the interactions between the cytoskeletal and the signaling system at the deformable

bioRxiv preprint doi: https://doi.org/10.1101/481887; this version posted June 12, 2019. The copyright holder for this preprint (which was not certified by peer review) is the author/funder. All rights reserved. No reuse allowed without permission.

membrane. The behavior of the two sub-systems when isolated can be conceptualized with paradigmatic reaction-diffusion models, where self-amplification of local structures triggers depletion of its free substrate. Both can independently break symmetry reflecting spontaneous polar protrusion GUV morphology (Figure 1), or self-organized SspB-AuroraB patterning (Figures 2C – 2E). However, a joint dynamical system is established in SynMMS, where the MT-induced membrane deformation enhances SspB-AuroraB translocation and thereby its activity, that in turn locally promotes the MT-growth (Figure 5B). Reaction-diffusion simulations of the coupled system demonstrated that the star-like morphology is generated when the rate of self-amplified AuroraB clustering on the membrane is greater than the local amplification rate of free MTs in the SIC protrusions (Figure S6F, left). In contrast, for the same total concentrations but inversed strength of the auto-amplification rates, the system evolved towards a single stable SIC protrusion (Figure S6F, right). This implies that the basal activity of the signaling system in absence of a stimulus accounts for the differences in initial morphologies between SynMMS and the encapsulated cytoskeletal system alone (Figure 5A). Thus, when the self-amplifying SspB-AuroraB clustering rate is dominant, the initial morphology is dictated by the total SspB-AuroraB concentration on the membrane. Bifurcation analysis indeed showed that the SspB-AuroraB concentration on the membrane determines if the system can break symmetry and thereby acquires self-organized shapes (Figure 5C). The system with a SspB-AuroraB membrane concentration that is lower than that of the symmetry-breaking pitchfork bifurcation corresponds to a spherical morphology with small aster size, whereas for concentrations above this point, the system either self-organizes to polar (organization in the vicinity of the bifurcation) or star-like morphologies (after the bifurcation).

Although the abstraction of this paradigmatic model only permits the description of global morphological effects without the details of centrosome repositioning, we also investigated the limits of morphological plasticity to global or local signals as a function of the initial shape and difference in auto-amplification rates of both sub-systems. Global stimulus corresponding to global light illumination that increases the amount of free AuroraB monomers on the membrane and thereby enhances the cooperative clustering did neither affect the initial polar nor star morphology, and only widened and further stabilized the pre-existing protrusions (Figures 5D). Local signal input to an intital multi-protrusion star-like morphology however led to global re-organization of the protrusions. The simulation demonstrated that the neighboring protrusions coalesced in the signal region, resulting in a star-to-polar morphological transition (Figure 5E). This can be understood in terms of effective depletion of MTs from other protrusions in response to the localized signal.

In order to test whether the size of the protrusions can limit the plasticity of star-like morphologies, we used the coupled system where the MTs self-amplification rate exceeds that of AuroraB and pre-patterned the initial state to generate an initial star morphology with four strong protrusions. Although neighboring protrusions converged to a single one upon the first local stimulus, no morphological change could be triggered with a subsequent, differently localized stimulus (Figure 5F). These results therefore suggest that the signaling strength at the plasma membrane confers plasticity to morphological responses, whereas strong SIC protrusions constrain the morphological transitions. To investigate the interplay between these two factors, we pre-patterned the initial state of the coupled system with dominant SspB-AuroraB self-amplification rate, to have one major and few smaller SIC protrusions on the opposite side. The simulations demonstrated limited responsiveness to subsequent signals, such that the stabilization of the major protrusion was promoted (Figure 5G). Taken together, these numerical findings suggest that star-like morphologies resulting from the recursive interactions between the signaling and the cytoskeletal system have highest morphogenic plasticity to local morphogen signals, whereas strong SIC protrusions confer robustness to shapes.

bioRxiv preprint doi: https://doi.org/10.1101/481887; this version posted June 12, 2019. The copyright holder for this preprint (which was not certified by peer review) is the author/funder. All rights reserved. No reuse allowed without permission.

Light-induced morphological state transitions

We assessed experimentally how the different initial morphological states of SynMMS limit morphological responsiveness to light stimuli. We first investigated the morphological responses of a polar SynMMS to step-wise increase in global light illumination (Figures 6A – 6C; Video S6). In this case, SspB-AuroraB was preferentially recruited to pre-existing protrusions, even at very low light-doses (Figures 6A and 6C). This is consistent with enhanced signaling from strongly deformed membrane areas that in turn enhance MT-growth and their ability to deform the membrane. This led to a light-dose dependent broadening of the main protrusion, in accordance with the numerical findings (Figure 5D, left). Enhanced MT-growth in the main protrusion was also apparent from centrosome displacement further away from it (Figures 6B and 6C). This demonstrates that SynMMS, which previously underwent spontaneous symmetry breaking into a polar morphology will reinforce its state upon global stimulation.

Increasing the light-dose illumination of star-like SynMMS also enhanced growth of MTs in pre-existing protrusions, resulting in their strong bending (Figures 6D – 6F; Video S6). However, the protrusions approximately maintained their initial positioning, although the enhanced MT-growth strongly decentered the centrosome. This again shows that enhanced signaling in pre-deformed membrane areas stabilizes protrusions, in accordance with the numerical results (Figure 5D, right). However, in contrast to an initial polar morphology, the growth of MTs in the protrusions of a star-like SynMMS enables strong centrosome decentering and thereby promotes a transition to a spherical morphology with cortical MTs. We observed such decentering behavior in a set SynMMS, but not in SynMMS$^{\text{-stat}}$ (Figure S6G). Overall, this shows that spontaneous membrane protrusions are robustly maintained upon global stimuli due to the recursive interactions between AuroraB-mediated signaling and MT-growth. This limits the morphological transitions induced by global activation of signaling in agreement with the numerical findings.

However, our theoretical findings suggested that star-like initial states exhibit the highest morphogenic plasticity to local stimuli (Figures 5E – 5G). We therefore next mimicked exposure of a cell to an external morphogen gradient by locally irradiating a set of star-like SynMMS (Figure 7). We first stimulated a star-like SynMMS with initially isotropically distributed small protrusions with few MTs, indicative of strong basal SspB-AuroraB activity. During continuous illumination in a localized region, pre-existing flanking membrane protrusions converged into this area, as theoretically predicted (Figures 7A – 7C; Video S7, compare to Figure 5E). Furthermore, as the protrusions migrated into the illuminated area with high SspB-AuroraB activity, MT-growth was further amplified leading to sprouting of additional micro-protrusions (Figure 7A; Video S7). This was accompanied by an overall morphing process that went from star-like into a polar morphology and resulted in a global reorientation towards the irradiated region, demonstrating that star-like SynMMS can exhibit a directed response to a localized stimulus (Figures 7A and 7B).

We next investigated the morphogenic plasticity of a star-like SynMMS whose shape was stabilized by four strong SIC protrusions (Figures 7D – 7F; Video S7). During local irradiation between two SIC protrusions, we observed the coalescence of a smaller SIC-protrusion into the larger one. This shows that SIC protrusions constantly exchange MTs with the rest of the system and can be therefore reorganized by a local tubulin gradient between them that promotes growth of nearby escaped MTs. Since the escape rate is likely higher for MTs in a small SIC protrusion, it will be assimilated into the larger one. However, subsequent irradiation between the newly enhanced and the neighboring large SIC protrusion did not trrigger their coalescence. This suggest that large protrusions are stabilized due to a slow escape rate of the MTs, rendering them robust to local light stimuli, in agreement with the numerical findings that the morphogenic plasticity of SynMMS will be constrained by the presence of large SIC protrusions (Figure 5F).

bioRxiv preprint doi: https://doi.org/10.1101/481887; this version posted June 12, 2019. The copyright holder for this preprint (which was not certified by peer review) is the author/funder. All rights reserved. No reuse allowed without permission.

To next investigate how the morphogenic plasticity of a star-like SynMMS is affected by a pronounced pre-existing protrusion, we sequentially irradiated the flanks of a star-like SynMMS with such a protrusion (Figures 7G and 7H; Video S7). Upon irradiating the left side area, the SynMMS rotated in the direction of the signal, showing that the overall MT-growth was promoted towards the irradiated area. The most pronounced morphological change was observed above the irradiated area in the vicinity of the major protrusion that itself broadened, indicative of MTs moving into it. Upon sequentially irradiating the opposite side in the same SynMMS, the direction of its rotation perpendicular to the main axis was reverted, caused by enhanced MT-growth towards the light source and amplification of signaling, apparent from the SspB-AuroraB recruitment in local membrane deformations (Figure 7H). These self-amplified protrusions were sliding towards the main-axis protrusion, which was accompanied by the clear loss of the lower right protrusion. This became even more apparent upon subsequent global irradiation of this SynMMS, where the assimilation of the gliding local protrusions into the main-axis protrusion could be clearly observed (Video S7). However, in this case, we also observed the formation of new protrusions flanking the reinforced main one, that were stabilized by self-amplification, as apparent from the SspB-AuroraB recruitment (Figure 7G). Numerical simulations describing the effect of sequential flanking activation on a pre-patterned system with a major protrusion opposite of three clustered smaller protrusions, were in agreement with this conclusion (Figure 5G). These results thereby show that a localized stimulus can evoke a global morphological transition in SynMMS. However, the directionality of this process is dictated by the prior morphological state. In an initial morphology that is stabilized by basal signaling activity, the accelerated growth of few MTs is sufficient for the maintenance of protrusions. This leaves enough free MTs to continuously reorient existing protrusions in the direction of external signals to be eventually locked in by strong amplification of signaling. In contrast, dominant SIC protrusions constrain this morphological plasticity by acting as strong MT sinks.

DISCUSSION

To distill basic principles of morphogen-guided cell morphogenesis, we reconstituted dynamic microtubule asters inside GUVs together with a signaling system that is actuated by dimensionality reduction and operates under non-equilibrium conditions. We found that light-induced translocation of SspB-AuroraB induces a stathmin phosphorylation/dephosphorylation cycle near membrane, thereby enhancing the local tubulin concentration which promotes MT growth. Such a tubulin pump could serve as a generic mechanism for directed MT-growth, e.g. guiding MTs to kinetochores during pro-metaphase in mitosis, where AuroraB localized on centromeres drives stathmin phosphorylation (Gadea and Ruderman, 2006; Wang et al., 2011). This coupling between the plasma membrane signaling and MT-dynamics is however not uni-directional. We identified that the reverse causality is also established, thereby generating interdependence between signaling and MT-cytoskeleton, enabling spontaneous morphogenesis to occur. Our findings identified the deformable membrane as a key mediator of these recursive interactions, suggesting that this mechanism universally occurs in mammalian cells. We could demonstrate that this simple system without biochemical reaction mediated feedback already has self-organized morphogenic abilities based on the principle of local matter coalescence through self-amplification, which in turn depletes the substrate from the surrounding. This is analogous to Grassé's stigmergic concept of collective behavior of social insects through indirect communication (Grassé, 1959). The question is why cells would harness this self-organized morphogenic mechanism to regulate their shape. During differentiation, the cohesively organized MT-network not only generates but also maintains the adopted cell shape, as for example in axon formation during neurogenesis (Kapitein and

bioRxiv preprint doi: https://doi.org/10.1101/481887; this version posted June 12, 2019. The copyright holder for this preprint (which was not certified by peer review) is the author/funder. All rights reserved. No reuse allowed without permission.

Hoogenraad, 2015). This requires both plasticity in shape formation by undifferentiated cells dependent on directional environmental cues, but also shape stabilization after the initial morphogen cue has dissipated. Although many layers of biochemical regulation likely contribute to both morphological plasticity and stabilization in cells (Akhmanova and Steinmetz, 2008; Watanabe et al., 2005), we demonstrate that the recursive interaction of MTs with signaling at the deformable membrane is sufficient to fulfill both requirements.

Our observations that the initial star-morphology is the most plastic, whereas the polar the most robust one, lead to the question how cells can switch between plasticity and stabilization of shapes. In this sense, the interplay between actin and MTs may be of fundamental importance, where actin would generate rapid and local morphological dynamics at the cell periphery, while the MT-cytoskeleton would guide the global shape. This could be further elucidated using synthetic systems that build upon SynMMS. In fact, a growing number of encapsulation techniques is becoming widely available, which allow creation of synthetic systems with deformable lipid bilayers, as opposed to previously often employed rigid water-in-oil droplets (Abkarian et al., 2011; Karamdad et al., 2015; Petit et al., 2016; Stachowiak et al., 2008). Progress has been also made in reconstituting actin networks on and within synthetic membranes (Guevorkian et al., 2015; Su et al., 2016). Importantly, more is becoming known about the crosstalk between actin and microtubules from studies in cells (Dogterom and Koenderink, 2019), and first steps have been made to crosslink the two systems or trigger MT nucleation by actin self-organization (Colin et al., 2016; Preciado López et al., 2014). Actin and microtubules also crosstalk via shared regulators, most of which are members of the Rho family of small GTPases, enabling many possible designs of coupled synthetic systems. Furthermore, curvature generating and sensing BAR domains contain catalytic domains that link to Rho GTPases, thereby generating an additional layer of recursion between membrane deformation and signaling (Ahmed et al., 2010; de Kreuk and Hordijk, 2012; Salzer et al., 2017). An additional step would be the inclusion of MT-interacting motor proteins, such as dynein and kinesins, that can further affect the self-organization of MTs by regulating MT dynamics and bundling (Bieling et al., 2010a; Gardner et al., 2011; Laan et al., 2012).

At the higher scale, first steps have been made to generate synthetic tissues where porous proto-cells communicate by diffusive protein signals to form larger tissue-mimicking arrays (Niederholtmeyer et al., 2018). The communication in these synthetic systems was based on a uni-directional causality with distinct signal emitter and receiver synthetic cells. The intrinsic self-organizing morphological dynamics of SynMMS has the potential to generate new morphologies that differ from the single synthetic systems by recursive communication between SynMMS (Koseska and Bastiaens, 2017). This will enable the investigation of self-organized tissue formation and establishment of cellular identity.

The short life span of SynMMS is constrained by the encapsulated fuel store (ATP, GTP). By equipping SynMMS with an artificial photosynthetic membrane (Steinberg-Yfrach et al., 1998), light energy could be converted into ATP or even GTP chemical potential that could maintain its non-equilibrium state over prolonged periods. Finally, recent progress in reconstituting self-replicating DNA by its encoded proteins in liposomes (van Nies et al., 2018), bacterial cell division (Litschel et al., 2018) and lipid metabolism (Scott et al., 2016) suggests that self-replicating properties could be conferred to synthetic systems such as SynMMS in the future.

STAR METHODS

Detailed methods are provided in the online version of this paper and include the following:

bioRxiv preprint doi: https://doi.org/10.1101/481887; this version posted June 12, 2019. The copyright holder for this preprint (which was not certified by peer review) is the author/funder. All rights reserved. No reuse allowed without permission.

SUPPLEMENTAL INFORMATION

Supplemental Information includes eight figures, one table, seven videos and can be found with this article online

ACKNOWLEDGMENTS

The authors thank Peter Bieling for reagents, helpful discussions and help in shaping the manuscript, Roger Goody for assistance with the stopped-flow experiments, H. Schütz, K. Michel, M. Reichl, and S. Gentz for technical assistance and A. Krämer for critical reading of the manuscript. This project was funded by the BMBF/MPG network MaxSynBio (031A359A).

AUTHOR CONTRIBUTIONS

K.G. developed biochemical assays as well as COPY^{o}, purified and encapsulated proteins, performed biochemical and imaging experiments. F.G. generated encapsulated asters, performed MT assays and imaging experiments, B.S. developed and performed image and morphometric analysis, A.N. and M.C.M. performed numerical simulations, H.S. performed biochemical assays and imaging experiments, M.S. developed and performed gradient reaction-diffusion simulations, A.K. & P.B. developed theoretical concepts, P.B. conceived and supervised the project and wrote the manuscript with help of A.K., B.S. and K.G. All authors provided input to the preparation of the manuscript.

DECLARATION OF INTERESTS

The authors declare no competing interests.

REFERENCES

Abkarian, M., Loiseau, E., and Massiera, G. (2011). Continuous droplet interface crossing encapsulation (cDICE) for high throughput monodisperse vesicle design. Soft Matter *7*, 4610.

bioRxiv preprint doi: https://doi.org/10.1101/481887; this version posted June 12, 2019. The copyright holder for this preprint (which was not certified by peer review) is the author/funder. All rights reserved. No reuse allowed without permission.

Adam, G., and Delbrück, M. (1968). Reduction of dimensionality in biological diffusion processes. In Structural Chemistry and Molecular Biology, (San Francisco: W. H. Freeman and Co.), pp. 198–215.

Ahmed, S., Bu, W., Lee, R.T.C., Maurer-Stroh, S., and Goh, W.I. (2010). F-BAR domain proteins: Families and function. Commun. Integr. Biol. *3*, 116–121.

Akhmanova, A., and Steinmetz, M.O. (2008). Tracking the ends: a dynamic protein network controls the fate of microtubule tips. Nat. Rev. Mol. Cell Biol. *9*, 309–322.

Baumann, H., and Surrey, T. (2014). Motor-mediated cortical versus astral microtubule organization in lipid-monolayered droplets. J. Biol. Chem. *289*, 22524–22535.

Bieling, P., Telley, I.A., and Surrey, T. (2010a). A minimal midzone protein module controls formation and length of antiparallel microtubule overlaps. Cell *142*, 420–432.

Bieling, P., Telley, I.A., Hentrich, C., Piehler, J., and Surrey, T. (2010b). Fluorescence microscopy assays on chemically functionalized surfaces for quantitative imaging of microtubule, motor, and +TIP dynamics. Methods Cell Biol. *95*, 555–580.

Bornens, M., and Moudjou, M. (1999). Studying the composition and function of centrosomes in vertebrates. Methods Cell Biol. *61*, 13–34.

Castoldi, M., and Popov, A.V. (2003). Purification of brain tubulin through two cycles of polymerization-depolymerization in a high-molarity buffer. Protein Expr. Purif. *32*, 83–88.

Colin, A., Bonnemay, L., Gayrard, C., Gautier, J., and Gueroui, Z. (2016). Triggering signaling pathways using F-actin self-organization. Sci. Rep. *6*, 34657.

Curmi, P.A., Andersen, S.S., Lachkar, S., Gavet, O., Karsenti, E., Knossow, M., and Sobel, A. (1997). The stathmin/tubulin interaction in vitro. J. Biol. Chem. *272*, 25029–25036.

Daub, H., Gevaert, K., Vandekerckhove, J., Sobel, A., and Hall, A. (2001). Rac/Cdc42 and p65PAK regulate the microtubule-destabilizing protein stathmin through phosphorylation at serine 16. J. Biol. Chem. *276*, 1677–1680.

Dogterom, M., and Koenderink, G.H. (2019). Actin-microtubule crosstalk in cell biology. Nat. Rev. Mol. Cell Biol. *20*, 38–54.

Etienne-Manneville, S. (2004). Actin and microtubules in cell motility: which one is in control? Traffic Cph. Den. *5*, 470–477.

Etienne-Manneville, S. (2013). Microtubules in cell migration. Annu. Rev. Cell Dev. Biol. *29*, 471–499.

Etienne-Manneville, S., and Hall, A. (2002). Rho GTPases in cell biology. Nature *420*, 629–635.

Faivre-Moskalenko, C., and Dogterom, M. (2002). Dynamics of microtubule asters in microfabricated chambers: The role of catastrophes. Proc. Natl. Acad. Sci. *99*, 16788–16793.

Gadea, B.B., and Ruderman, J.V. (2006). Aurora B is required for mitotic chromatin-induced phosphorylation of Op18/Stathmin. Proc. Natl. Acad. Sci. U. S. A. *103*, 4493–4498.

bioRxiv preprint doi: https://doi.org/10.1101/481887; this version posted June 12, 2019. The copyright holder for this preprint (which was not certified by peer review) is the author/funder. All rights reserved. No reuse allowed without permission.

Gardner, M.K., Zanic, M., Gell, C., Bormuth, V., and Howard, J. (2011). Depolymerizing kinesins Kip3 and MCAK shape cellular microtubule architecture by differential control of catastrophe. Cell *147*, 1092–1103.

Gavriljuk, K., Itzen, A., Goody, R.S., Gerwert, K., and Kötting, C. (2013). Membrane extraction of Rab proteins by GDP dissociation inhibitor characterized using attenuated total reflection infrared spectroscopy. Proc. Natl. Acad. Sci. U. S. A. *110*, 13380–13385.

Grassé, P.-P. (1959). La Reconstruction du nid et les coordinations interindividuelles chez Bellicositermes natalensis et Cubitermes Sp. ; la théorie de la stigmergie : essai d'interprétation, comportement des termites constructeurs. Insectes Sociaux *6*, 41–81.

Grecco, H.E., Roda-Navarro, P., and Verveer, P.J. (2009). Global analysis of time correlated single photon counting FRET-FLIM data. Opt. Express *17*, 6493–6508.

Grecco, H.E., Roda-Navarro, P., Girod, A., Hou, J., Frahm, T., Truxius, D.C., Pepperkok, R., Squire, A., and Bastiaens, P.I.H. (2010). In situ analysis of tyrosine phosphorylation networks by FLIM on cell arrays. Nat. Methods *7*, 467–472.

Grieneisen, V. (2009). "Dynamics of auxin patterning in plant morphogenesis", thesis (University of Utrecht).

Guevorkian, K., Manzi, J., Pontani, L.-L., Brochard-Wyart, F., and Sykes, C. (2015). Mechanics of Biomimetic Liposomes Encapsulating an Actin Shell. Biophys. J. *109*, 2471–2479.

Guntas, G., Hallett, R.A., Zimmerman, S.P., Williams, T., Yumerefendi, H., Bear, J.E., and Kuhlman, B. (2015). Engineering an improved light-induced dimer (iLID) for controlling the localization and activity of signaling proteins. Proc. Natl. Acad. Sci. U. S. A. *112*, 112–117.

Howell, B., Larsson, N., Gullberg, M., and Cassimeris, L. (1999). Dissociation of the tubulin-sequestering and microtubule catastrophe-promoting activities of oncoprotein 18/stathmin. Mol. Biol. Cell *10*, 105–118.

Huber, F., Boire, A., López, M.P., and Koenderink, G.H. (2015). Cytoskeletal crosstalk: when three different personalities team up. Curr. Opin. Cell Biol. *32*, 39–47.

Hughes, L.D., Rawle, R.J., and Boxer, S.G. (2014). Choose Your Label Wisely: Water-Soluble Fluorophores Often Interact with Lipid Bilayers. PLoS ONE *9*, e87649.

Hyman, A., Drechsel, D., Kellogg, D., Salser, S., Sawin, K., Steffen, P., Wordeman, L., and Mitchison, T. (1991). Preparation of modified tubulins. Methods Enzymol. *196*, 478–485.

Janson, M.E., de Dood, M.E., and Dogterom, M. (2003). Dynamic instability of microtubules is regulated by force. J. Cell Biol. *161*, 1029–1034.

Juniper, M.P.N., Weiss, M., Platzman, I., Spatz, J.P., and Surrey, T. (2018). Spherical network contraction forms microtubule asters in confinement. Soft Matter *14*, 901–909.

Kapitein, L.C., and Hoogenraad, C.C. (2015). Building the Neuronal Microtubule Cytoskeleton. Neuron *87*, 492–506.

bioRxiv preprint doi: https://doi.org/10.1101/481887; this version posted June 12, 2019. The copyright holder for this preprint (which was not certified by peer review) is the author/funder. All rights reserved. No reuse allowed without permission.

Karamdad, K., Law, R.V., Seddon, J.M., Brooks, N.J., and Ces, O. (2015). Preparation and mechanical characterisation of giant unilamellar vesicles by a microfluidic method. Lab Chip *15*, 557–562.

Koseska, A., and Bastiaens, P.I. (2017). Cell signaling as a cognitive process. EMBO J. *36*, 568–582.

de Kreuk, B.-J., and Hordijk, P.L. (2012). Control of Rho GTPase function by BAR-domains. Small GTPases *3*, 45–52.

Laan, L., Roth, S., and Dogterom, M. (2012). End-on microtubule-dynein interactions and pulling-based positioning of microtubule organizing centers. Cell Cycle Georget. Tex *11*, 3750–3757.

Letort, G., Nedelec, F., Blanchoin, L., and Théry, M. (2016). Centrosome centering and decentering by microtubule network rearrangement. Mol. Biol. Cell *27*, 2833–2843.

Leung, T., Manser, E., Tan, L., and Lim, L. (1995). A novel serine/threonine kinase binding the Ras-related RhoA GTPase which translocates the kinase to peripheral membranes. J. Biol. Chem. *270*, 29051–29054.

Litschel, T., Ramm, B., Maas, R., Heymann, M., and Schwille, P. (2018). Beating vesicles: Encapsulated protein oscillations cause dynamic membrane deformations. Angew. Chem. Int. Ed Engl.

Manser, E., Leung, T., Salihuddin, H., Zhao, Z.S., and Lim, L. (1994). A brain serine/threonine protein kinase activated by Cdc42 and Rac1. Nature *367*, 40–46.

Marée, A.F.M., Jilkine, A., Dawes, A., Grieneisen, V.A., and Edelstein-Keshet, L. (2006). Polarization and movement of keratocytes: a multiscale modelling approach. Bull. Math. Biol. *68*, 1169–1211.

Marwan, N., Carmenromano, M., Thiel, M., and Kurths, J. (2007a). Recurrence plots for the analysis of complex systems. Phys. Rep. *438*, 237–329.

Marwan, N., Kurths, J., and Saparin, P. (2007b). Generalised recurrence plot analysis for spatial data. Phys. Lett. A *360*, 545–551.

Mitchison, T., and Kirschner, M. (1984). Dynamic instability of microtubule growth. Nature *312*, 237–242.

Mocenni, C., Facchini, A., and Vicino, A. (2010). Identifying the dynamics of complex spatio-temporal systems by spatial recurrence properties. Proc. Natl. Acad. Sci. *107*, 8097–8102.

Muroyama, A., and Lechler, T. (2017). Microtubule organization, dynamics and functions in differentiated cells. Dev. Camb. Engl. *144*, 3012–3021.

Nédélec, F.J., Surrey, T., Maggs, A.C., and Leibler, S. (1997). Self-organization of microtubules and motors. Nature *389*, 305–308.

Niederholtmeyer, H., Chaggan, C., and Devaraj, N.K. (2018). Communication and quorum sensing in non-living mimics of eukaryotic cells. Nat. Commun. *9*.

bioRxiv preprint doi: https://doi.org/10.1101/481887; this version posted June 12, 2019. The copyright holder for this preprint (which was not certified by peer review) is the author/funder. All rights reserved. No reuse allowed without permission.

van Nies, P., Westerlaken, I., Blanken, D., Salas, M., Mencía, M., and Danelon, C. (2018). Self-replication of DNA by its encoded proteins in liposome-based synthetic cells. Nat. Commun. *9*, 1583.

Niethammer, P., Bastiaens, P., and Karsenti, E. (2004). Stathmin-tubulin interaction gradients in motile and mitotic cells. Science *303*, 1862–1866.

Oancea, E., and Meyer, T. (1998). Protein kinase C as a molecular machine for decoding calcium and diacylglycerol signals. Cell *95*, 307–318.

Petit, J., Polenz, I., Baret, J.-C., Herminghaus, S., and Bäumchen, O. (2016). Vesicles-on-a-chip: A universal microfluidic platform for the assembly of liposomes and polymersomes. Eur. Phys. J. E Soft Matter *39*, 59.

Pinot, M., Chesnel, F., Kubiak, J.Z., Arnal, I., Nedelec, F.J., and Gueroui, Z. (2009). Effects of confinement on the self-organization of microtubules and motors. Curr. Biol. CB *19*, 954–960.

Popp, M.W., Antos, J.M., Grotenbreg, G.M., Spooner, E., and Ploegh, H.L. (2007). Sortagging: a versatile method for protein labeling. Nat. Chem. Biol. *3*, 707–708.

Preciado López, M., Huber, F., Grigoriev, I., Steinmetz, M.O., Akhmanova, A., Koenderink, G.H., and Dogterom, M. (2014). Actin-microtubule coordination at growing microtubule ends. Nat. Commun. *5*, 4778.

Rangamani, P., Lipshtat, A., Azeloglu, E.U., Calizo, R.C., Hu, M., Ghassemi, S., Hone, J., Scarlata, S., Neves, S.R., and Iyengar, R. (2013). Decoding information in cell shape. Cell *154*, 1356–1369.

Salzer, U., Kostan, J., and Djinović-Carugo, K. (2017). Deciphering the BAR code of membrane modulators. Cell. Mol. Life Sci. CMLS *74*, 2413–2438.

Schmick, M., Vartak, N., Papke, B., Kovacevic, M., Truxius, D.C., Rossmannek, L., and Bastiaens, P.I.H. (2014). KRas localizes to the plasma membrane by spatial cycles of solubilization, trapping and vesicular transport. Cell *157*, 459–471.

Scott, A., Noga, M.J., de Graaf, P., Westerlaken, I., Yildirim, E., and Danelon, C. (2016). Cell-Free Phospholipid Biosynthesis by Gene-Encoded Enzymes Reconstituted in Liposomes. PloS One *11*, e0163058.

Sendra, G.H., Hoerth, C.H., Wunder, C., and Lorenz, H. (2015). 2D map projections for visualization and quantitative analysis of 3D fluorescence micrographs. Sci. Rep. *5*.

Sessa, F., Mapelli, M., Ciferri, C., Tarricone, C., Areces, L.B., Schneider, T.R., Stukenberg, P.T., and Musacchio, A. (2005). Mechanism of Aurora B activation by INCENP and inhibition by hesperadin. Mol. Cell *18*, 379–391.

Shen, K., and Meyer, T. (1999). Dynamic control of CaMKII translocation and localization in hippocampal neurons by NMDA receptor stimulation. Science *284*, 162–166.

Soheilypour, M., Peyro, M., Peter, S.J., and Mofrad, M.R.K. (2015). Buckling behavior of individual and bundled microtubules. Biophys. J. *108*, 1718–1726.

bioRxiv preprint doi: https://doi.org/10.1101/481887; this version posted June 12, 2019. The copyright holder for this preprint (which was not certified by peer review) is the author/funder. All rights reserved. No reuse allowed without permission.

Stachowiak, J.C., Richmond, D.L., Li, T.H., Liu, A.P., Parekh, S.H., and Fletcher, D.A. (2008). Unilamellar vesicle formation and encapsulation by microfluidic jetting. Proc. Natl. Acad. Sci. U. S. A. *105*, 4697–4702.

Steinberg-Yfrach, G., Rigaud, J.L., Durantini, E.N., Moore, A.L., Gust, D., and Moore, T.A. (1998). Light-driven production of ATP catalysed by F0F1-ATP synthase in an artificial photosynthetic membrane. Nature *392*, 479–482.

Su, X., Ditlev, J.A., Hui, E., Xing, W., Banjade, S., Okrut, J., King, D.S., Taunton, J., Rosen, M.K., and Vale, R.D. (2016). Phase separation of signaling molecules promotes T cell receptor signal transduction. Science *352*, 595–599.

Surrey, T., Nedelec, F., Leibler, S., and Karsenti, E. (2001). Physical properties determining self-organization of motors and microtubules. Science *292*, 1167–1171.

Thévenaz, P., Ruttimann, U.E., and Unser, M. (1998). A pyramid approach to subpixel registration based on intensity. IEEE Trans. Image Process. Publ. IEEE Signal Process. Soc. *7*, 27–41.

Thomas, F.A., Visco, I., Petrášek, Z., Heinemann, F., and Schwille, P. (2015). Introducing a fluorescence-based standard to quantify protein partitioning into membranes. Biochim. Biophys. Acta *1848*, 2932–2941.

Vignaud, T., Blanchoin, L., and Théry, M. (2012). Directed cytoskeleton self-organization. Trends Cell Biol. *22*, 671–682.

Wang, E., Ballister, E.R., and Lampson, M.A. (2011). Aurora B dynamics at centromeres create a diffusion-based phosphorylation gradient. J. Cell Biol. *194*, 539–549.

Watanabe, T., Noritake, J., and Kaibuchi, K. (2005). Regulation of microtubules in cell migration. Trends Cell Biol. *15*, 76–83.

Waterman-Storer, C.M., Worthylake, R.A., Liu, B.P., Burridge, K., and Salmon, E.D. (1999). Microtubule growth activates Rac1 to promote lamellipodial protrusion in fibroblasts. Nat. Cell Biol. *1*, 45–50.

Wittmann, T., Bokoch, G.M., and Waterman-Storer, C.M. (2003). Regulation of leading edge microtubule and actin dynamics downstream of Rac1. J. Cell Biol. *161*, 845–851.

Wu, S.-Z., and Bezanilla, M. (2018). Actin and microtubule cross talk mediates persistent polarized growth. J. Cell Biol. *217*, 3531–3544.

Zaytsev, A.V., Segura-Peña, D., Godzi, M., Calderon, A., Ballister, E.R., Stamatov, R., Mayo, A.M., Peterson, L., Black, B.E., Ataullakhanov, F.I., et al. (2016). Bistability of a coupled Aurora B kinase-phosphatase system in cell division. ELife *5*, e10644.

bioRxiv preprint doi: https://doi.org/10.1101/481887; this version posted June 12, 2019. The copyright holder for this preprint (which was not certified by peer review) is the author/funder. All rights reserved. No reuse allowed without permission.

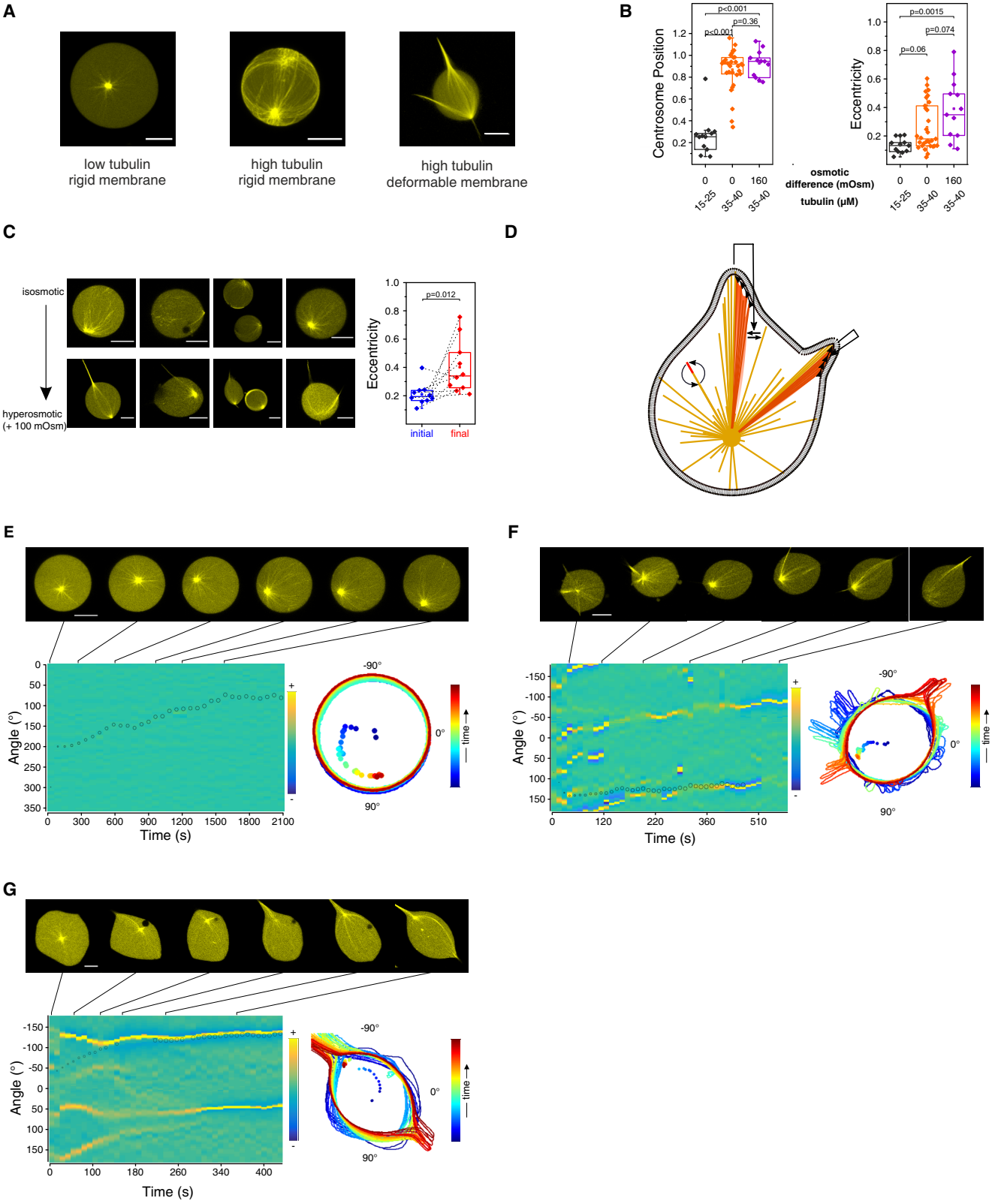

Figure 1. Interaction of astral MTs via the deformable membrane leads to self-organized polar morphology

(A) GUV morphologies, from left to right: small aster at low tubulin concentration (15 – 25 μM), cortical aster and polar morphologies at high tubulin (35 – 40 μM). Rightmost GUV at lowered membrane tension (hyperosmotic surrounding solution). (B) Morphometric quantification of GUVs with high or lowered membrane tension, and low or high tubulin concentration. Centrosome position: 0 – centered, 1 – membrane proximal, eccentricity: 0 – perfect circle, >0 – deviations from circle. Each dot corresponds to a GUV. p-values from two-sample Kolmogorov-Smirnov test. (C) Left: morphological transitions induced by membrane tension decrease caused by changing outside osmolarity (STAR Methods). Top and bottom

bioRxiv preprint doi: https://doi.org/10.1101/481887; this version posted June 12, 2019. The copyright holder for this preprint (which was not certified by peer review) is the author/funder. All rights reserved. No reuse allowed without permission.

rows show identical GUVs before and after osmolarity change. Right: corresponding morphometric quantification. Dashed lines connect initial and final states of single GUVs. p-values from two-sample Kolmogorov-Smirnov test. (D) Scheme of SIC protrusion formation. MT-induced membrane deformation promotes capture of neighboring MTs (straight arrows), which bundle by sliding into the protrusion (arrow heads). Curved arrows represent MT dynamic instability. (E) Snapshots of CLSM time-lapse of temperature-induced aster growth in a GUV with high membrane tension. Top: representative images from time-lapse, bottom left: kymograph of local membrane curvature with overlaid centrosome position (small circle: central, large circle: peripheral), bottom right: GUV contours during time-lapse, color coded by time progression (dots: corresponding centrosome position). (F) and (G) Snapshots of CLSM time-lapses of temperature-induced aster growth in GUVs with lowered membrane tension. Representation as in (E). Lines connect images with the corresponding time in the kymograph. Scale bars 10 µm. See also Figure S1.

bioRxiv preprint doi: https://doi.org/10.1101/481887; this version posted June 12, 2019. The copyright holder for this preprint (which was not certified by peer review) is the author/funder. All rights reserved. No reuse allowed without permission.

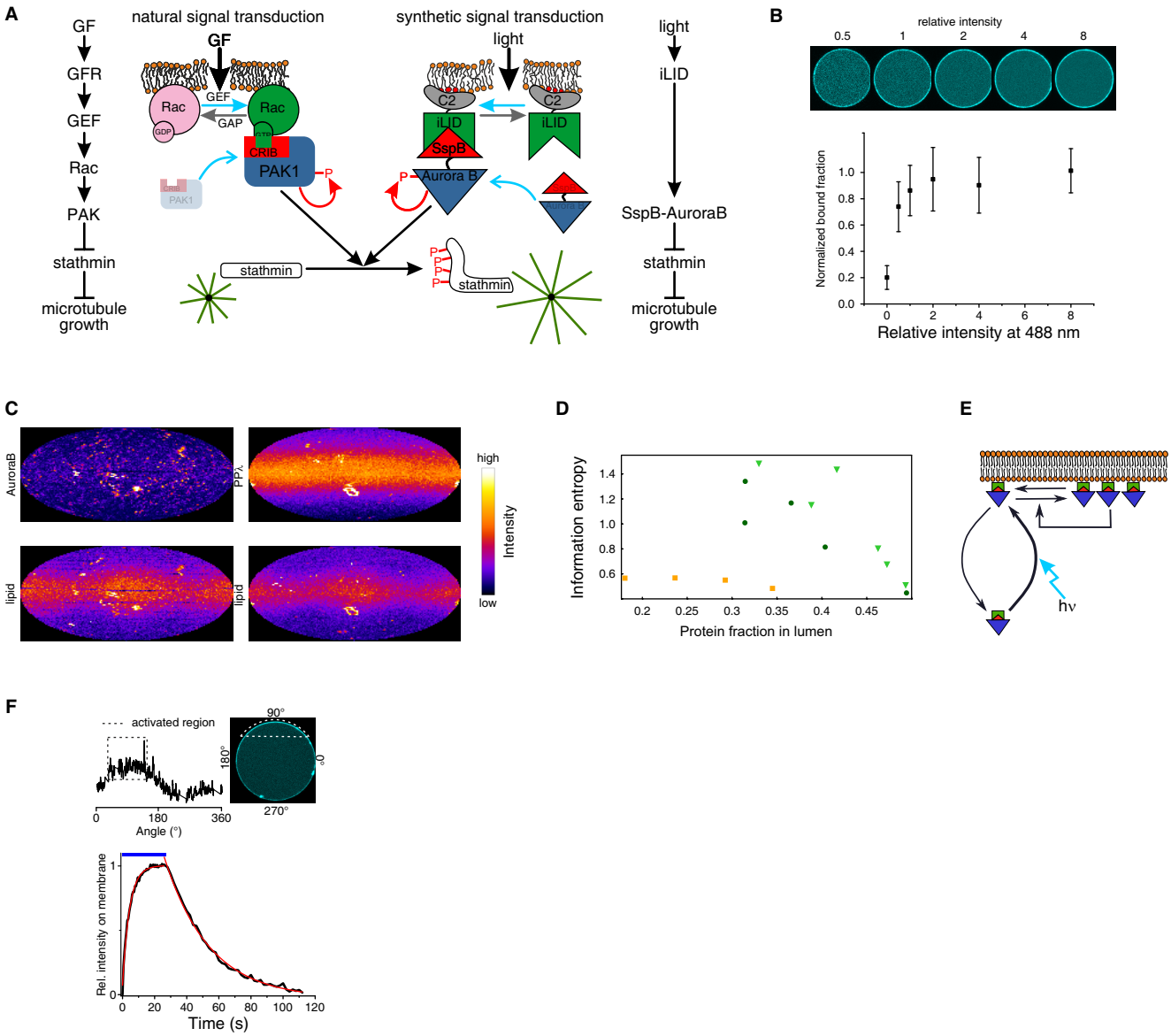

Figure 2. Light-induced SspB-AuroraB translocation and organization on GUV membrane

(A) Scheme of the natural and designed signaling system. Left and right: signaling pathways. GF: growth factor, GFR: growth factor receptor, GEF: guanine nucleotide exchange factor, Rac: small GTPase, PAK, AuroraB: serine threonine protein kinases, stathmin: MT regulator, iLID/SspB: improved light-inducible dimer and its binding partner, C2: phosphatidylserine binding domain. Center: corresponding activation (vertical black arrows) of natural or synthetic signal transduction by translocation of PAK to Rac·GTP (via CRIB domain) or SspB-AuroraB to C2-iLID on the membrane (curved blue arrows). Upon activation of kinase by autophosphorylation (red arrows) MT growth increases (green asters) by phosphorylation of stathmin (horizontal black arrow). (B) Bottom: light-dose response of SspB-AuroraB fraction recruited to the membrane (mean ± S.D. of 5 GUVs, 7 µM C2-iLID, 12 µM Alexa488-SspB-AuroraB). Top: corresponding example images. Laser power normalized to 65 mW/cm². (C) Surface intensity maps of translocated SspB-AuroraB (left) or SspB-PPλ (right) in representative GUVs. Bottom maps show the corresponding fluorescent LissamineRhodamineB-DOPE lipid distribution. (D) Respective recurrence quantification analysis of spatial protein pattern regularity (STAR Methods). Information entropy as function of protein depletion from GUV lumen is shown. Dark green: SspB-AuroraB with ATP, light green: –without ATP, orange: SspB-PPλ. Points correspond to individual GUVs. (E) Scheme of SspB-AuroraB (blue triangles) organization mechanism based on light-induced substrate-depletion (curved arrows) and cooperative (feedback arrow) clustering (horizontal arrows). (F)

bioRxiv preprint doi: https://doi.org/10.1101/481887; this version posted June 12, 2019. The copyright holder for this preprint (which was not certified by peer review) is the author/funder. All rights reserved. No reuse allowed without permission.

Top: SspB-AuroraB translocation gradient resulting from continuous blue light irradiation of a localized region (denoted by white dotted lines). Bottom: kinetics of light-induced membrane recruitment and release in absence of photo-activating light of Alexa647-SspB-AuroraB (global activation with 65 mW/cm² at 488 nm). Apparent rate constants: $k_{recruit}$ = 13.7 ± 0.3 min^{-1}, $k_{release}$ = 2.15 ± 0.06 min^{-1}. Data are mean of 4 GUVs. Scale bars 10 µm. See also Figure S2.

bioRxiv preprint doi: https://doi.org/10.1101/481887; this version posted June 12, 2019. The copyright holder for this preprint (which was not certified by peer review) is the author/funder. All rights reserved. No reuse allowed without permission.

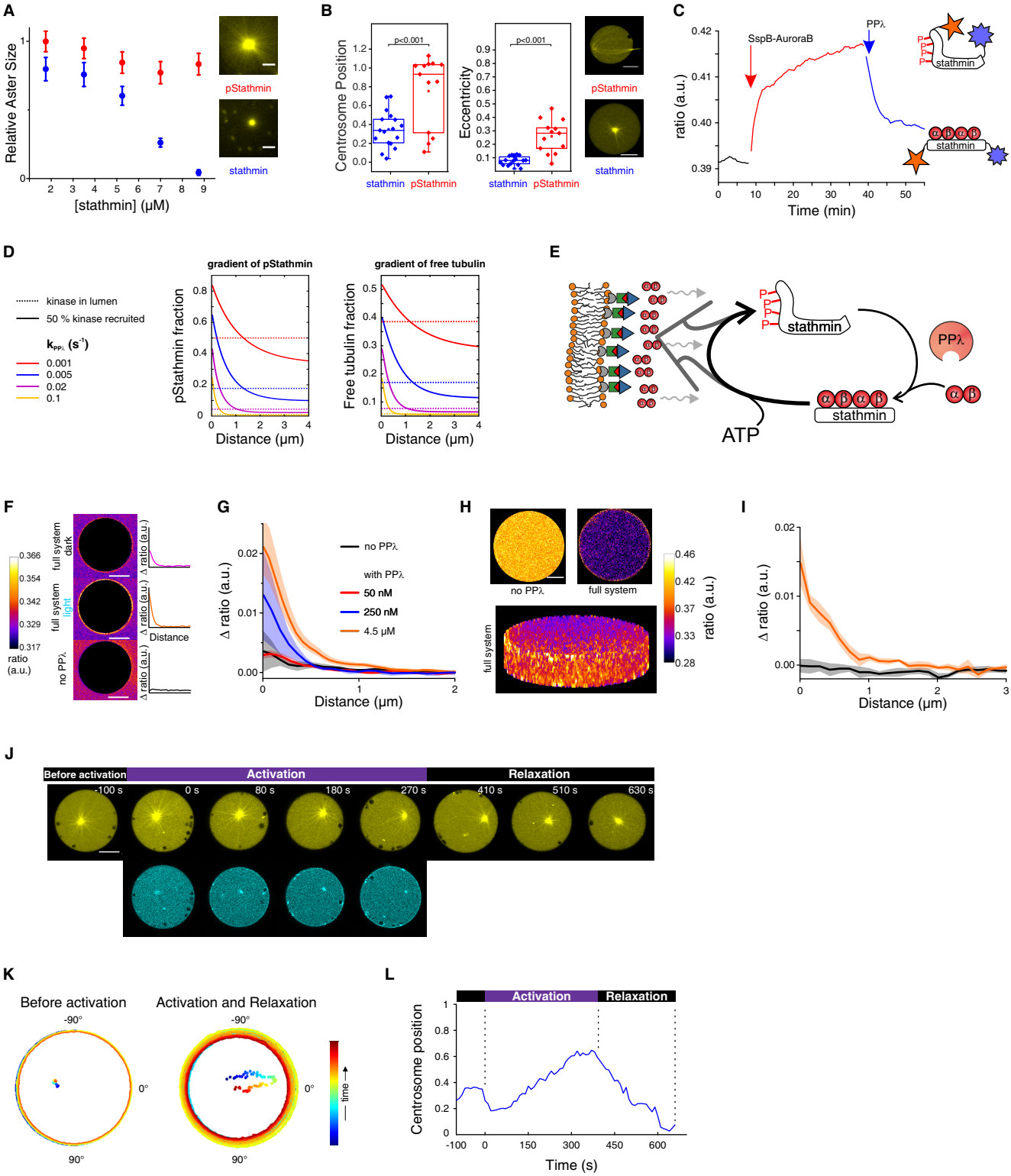

Figure 3. Signaling-induced membrane-proximal tubulin gradient regulates MT-aster size

(A) MT-aster size in solution as a function of stathmin (blue dots) and pStathmin (red dots) concentration at 35 μM tubulin. Error bars: Standard Error of the regression (STAR Methods). Images show examples of overlaid asters (> 30 asters per condition) at 35 μM tubulin and 7 μM pStathmin (top) or 7 μM stathmin (bottom). (B) GUV morphometric quantification (as in Figure 1B) demonstrating the effect of 5 μM stathmin or pStathmin on the morphology of encapsulated MT-asters (40 μM tubulin). Representative images on the right. p-values from two-sample Kolmogorov-Smirnov test. (C) Ratiometric measurement of sequential COPYº phosphorylation and dephosphorylation in bulk (10 μM COPYº, 20 μM tubulin, 2 μM SspB-AuroraB, 500 nM PPλ). Enzyme addition indicated by arrows. Right: scheme of the FRET-sensor COPYº in which stathmin was conjugated to Atto532 (orange) and Atto655 (violet). COPYº increases

bioRxiv preprint doi: https://doi.org/10.1101/481887; this version posted June 12, 2019. The copyright holder for this preprint (which was not certified by peer review) is the author/funder. All rights reserved. No reuse allowed without permission.

FRET efficiency by a conformational change that occurs by a phosphorylation induced release of αβ-tubulin heterodimers (red circles). (D) 1D reaction- diffusion simulation: pStathmin (middle) and free tubulin (right) concentration profiles from the membrane (0 µm) generated by stathmin phosphorylation cycle before (kinase only in lumen with k_{kin} = 0.004 s^{-1}, dashed lines) and after recruitment (50 % kinase on membrane with k_{kin} = 1 s^{-1}, solid lines) for varying $k_{PP\lambda}$ as indicated in the legend (left). Other parameters in STAR Methods. (E) Scheme of stathmin phosphorylation cycle maintaining an enhanced tubulin concentration near the membrane by the AuroraB kinase (blue triangles) driven release of tubulin (red circles) from stathmin near the membrane (dark gray arrow towards membrane), which is countered by diffusion away from the membrane (wiggly arrows). (F) Ratiometric images of COPY^o outside of GUVs with iLID on the membrane, SspB-AuroraB and tubulin in the bulk (concentrations in STAR Methods). Top: +250 nM PPλ in the absence of blue photo-activating light, center: after light-induced translocation of SspB-AuroraB, bottom: without PPλ, corresponding bulk ratio subtracted radial profiles (Δratio) to the right. (G) Quantification of Δratio gradients with different PPλ concentrations (mean ± S.E.M. of 4 GUVs for each condition). (H) COPY^o phosphorylation gradient inside GUVs. Top: maximum intensity projections of 8-slice ratiometric z-stacks without (left) and with PPλ (right), bottom: 3D-projection of the ratiometric z-stack with the full system. (I) Average of Δratio profiles inside GUVs. Without PPλ (black): mean ± S.E.M. of 6 GUVs, With PPλ (orange): mean ± S.E.M. of 4 GUVs. (J) Snapshots of CLSM time lapse of Alexa647-tubulin (yellow) and Alexa488-SspB-AuroraB (cyan) of a SynMMS with high membrane tension obtained before, during, and after global illumination with blue light. (K) Corresponding GUV contours for the entire time-lapse, color coded by time progression (dots: corresponding centrosome position). (L) Corresponding centrosome position plotted against time. 0 – centered, 1 – membrane proximal. Scale bars 10 µm. See also Figures S3 – S5.

bioRxiv preprint doi: https://doi.org/10.1101/481887; this version posted June 12, 2019. The copyright holder for this preprint (which was not certified by peer review) is the author/funder. All rights reserved. No reuse allowed without permission.

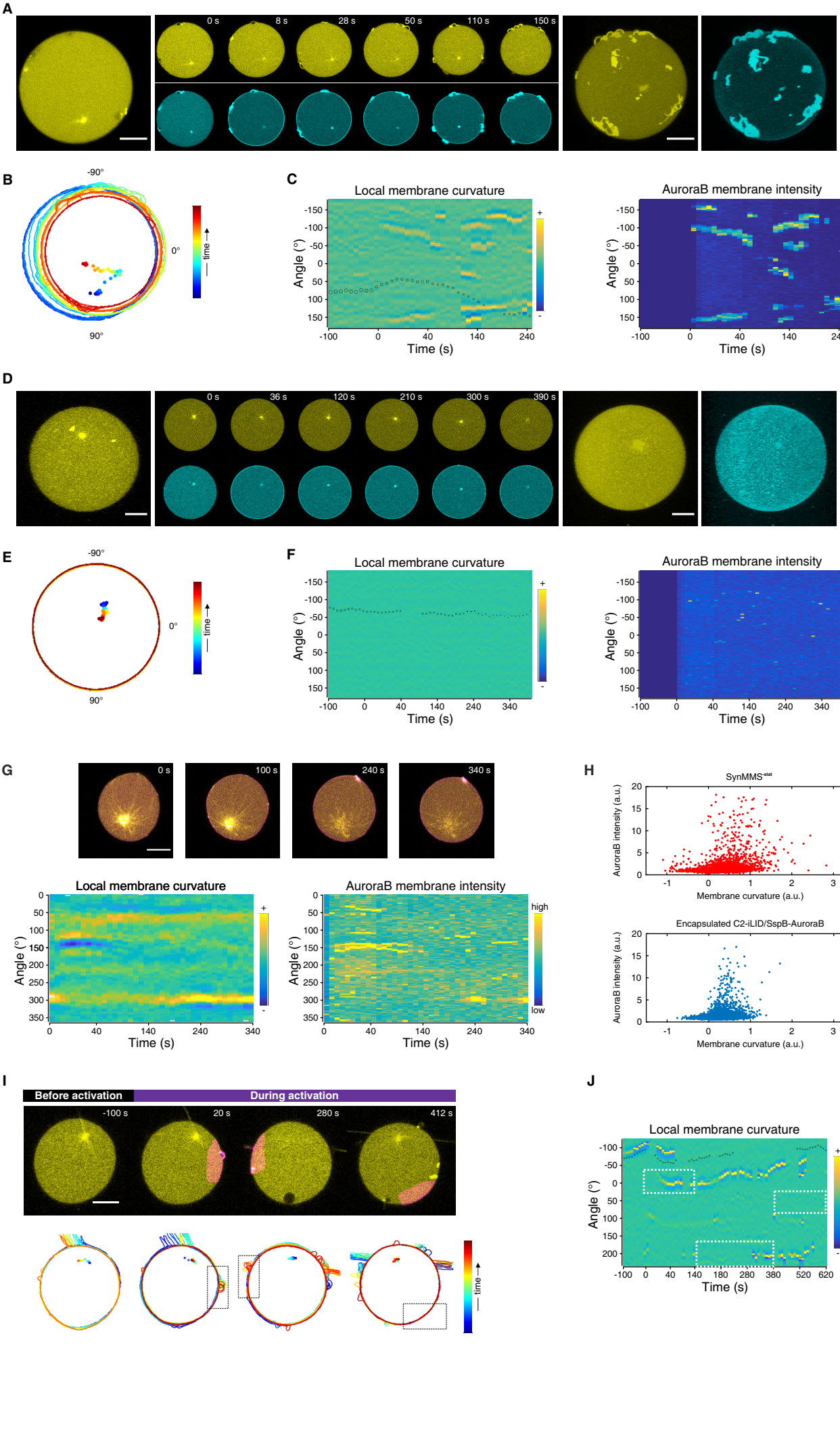

bioRxiv preprint doi: https://doi.org/10.1101/481887; this version posted June 12, 2019. The copyright holder for this preprint (which was not certified by peer review) is the author/funder. All rights reserved. No reuse allowed without permission.

Figure 4. Recursion between astral MTs and signaling at the deformable membrane generates a morphological memory

(A) Snapshots of CLSM time lapse of Alexa647-tubulin (yellow) and Alexa488-SspB-AuroraB (cyan) at the equatorial plane of a SynMMS with an initially small MT-aster during continuous global illumination with blue light. Maximum intensity projections of Alexa647-tubulin fluorescence of a confocal z-stack obtained before (left) and after (right, together with Alexa488-SspB-AuroraB) the time lapse series are shown. (B) Corresponding GUV contours for the entire time-lapse, color coded by time progression (dots: corresponding centrosome position). (C) Kymographs of local membrane curvature (left; with overlaid centrosome position, small circle: central, large circle: peripheral) and corresponding Alexa488-SspB-AuroraB membrane intensity (right) for SynMMS in (A). Negative time: prior to activation. (D) Snapshots of CLSM time lapse as above for a control SynMMS$^{\text{-stat}}$. (E) Corresponding contours and (F) kymographs. (G) Top row: snapshots of CLSM time lapse of Alexa647-tubulin (yellow) overlaid with Alexa488-SspB-AuroraB (magenta) at the equatorial plane of a SynMMS$^{\text{-stat}}$. Bottom: corresponding kymographs of local membrane curvature (left) and Alexa488-SspB-AuroraB membrane intensity (right). (H) Scatter plots of local membrane curvature versus Alexa488-SspB-AuroraB membrane intensity derived from a set of SynMMS$^{\text{-stat}}$ (top, Figure 4G and Figure S7) and a set of GUVs with encapsulated C2-iLID/SspB-AuroraB alone (bottom, same set as in Figure 2B). (I) Top row: snapshots of CLSM time lapse of Alexa647-tubulin (yellow) overlaid with Alexa488-SspB-AuroraB (magenta) at the equatorial plane of a SynMMS sequentially activated in different areas. Bottom row: GUV contours corresponding to above phases. Rectangles mark activation regions. (J) Corresponding kymograph of local membrane curvature. Scale bars 10 µm. See also Figures S6 – S8.

bioRxiv preprint doi: https://doi.org/10.1101/481887; this version posted June 12, 2019. The copyright holder for this preprint (which was not certified by peer review) is the author/funder. All rights reserved. No reuse allowed without permission.

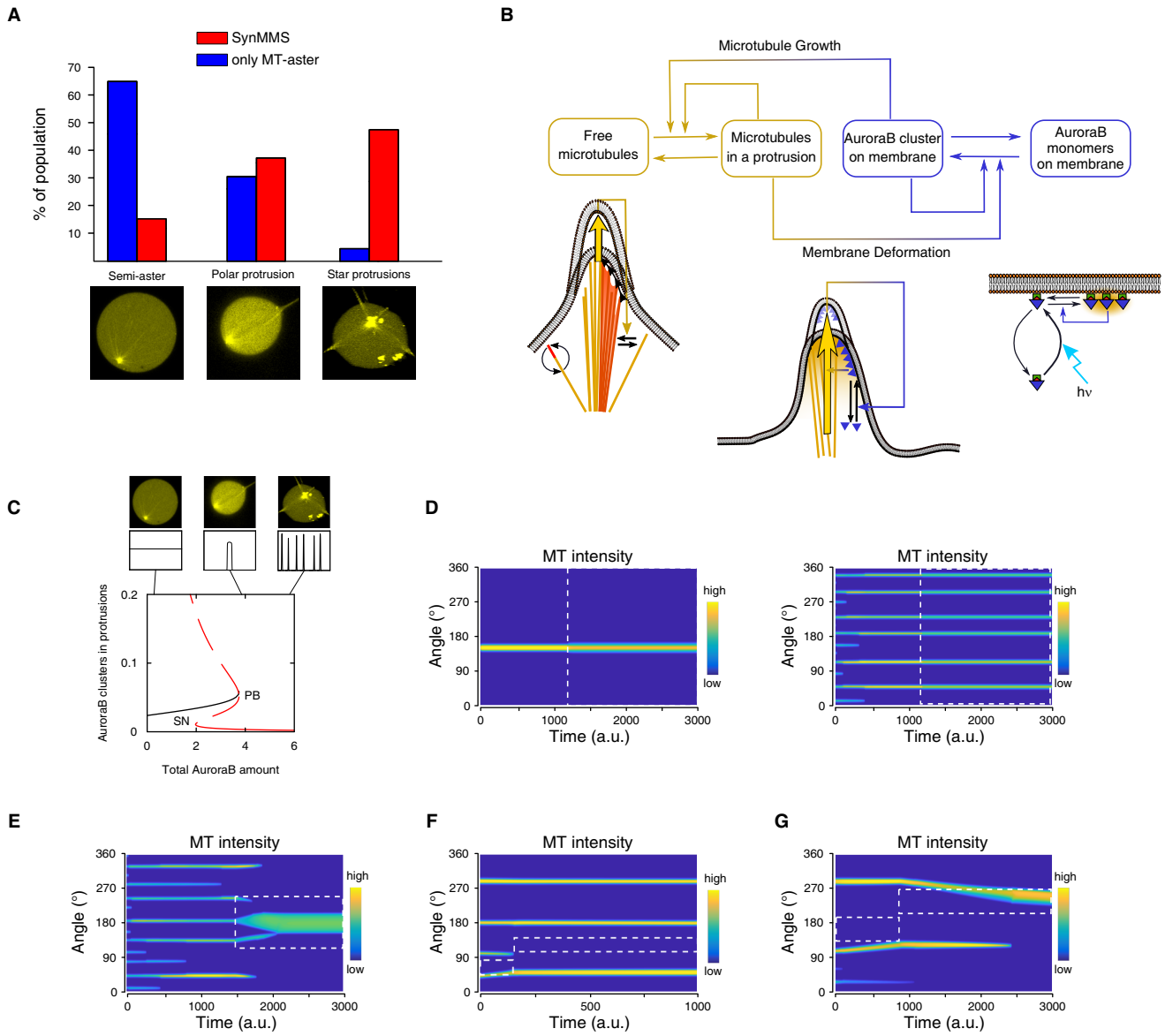

Figure 5. Paradigmatic reaction-diffusion model of SynMMS morphogenesis

(A) Classification of experimentally obtained SynMMS (red) and encapsulated MT-asters (blue) morphologies in the absence of stimulus. Representative images of the three main classes shown below. (B) Scheme of the MT-aster/membrane (lower left, as in Figure 1D) and AuroraB sub-system (lower right, as in Figure 2E), as well as the joint dynamical system established in SynMMS (top and middle low). Membrane-proximal tubulin gradient shown in yellow. (C) Bifurcation diagram of the generalized substrate-depletion model of the full system depicted in (B). Bifurcations: PB - pitchfork, SN - saddle-node. Solid lines: stable homogenous (black) and symmetry broken (red) solution. Dashed line: unstable solution. Top: representative images and numerical distribution of spatial structures at indicated parameter positions in the diagram. (D) Numerically obtained kymographs of MT protrusions (MT intensity) depicting the temporal evolution of a polar (left) and star-like (right) initial morphologies subjected to global external signal. White dashed rectangles mark activation regions in (D) – (G). (E) Local signal induces a star-to-polar morphological transition, as depicted by a numerically obtained MT intensity kymograph. (F) Numerical MT intensity kymograph indicating limits of plasticity of a pre-patterned star-like morphology to subsequent spatially separated signals. (G) Strong SIC-protrusion constrains and thereby dominates the morphology. The numerical MT intensity kymograph demonstrates broadening of the strong protrusion, as the remaining smaller protrusions are lost. All respective parameters in STAR Methods. See also Figure S6.

bioRxiv preprint doi: https://doi.org/10.1101/481887; this version posted June 12, 2019. The copyright holder for this preprint (which was not certified by peer review) is the author/funder. All rights reserved. No reuse allowed without permission.

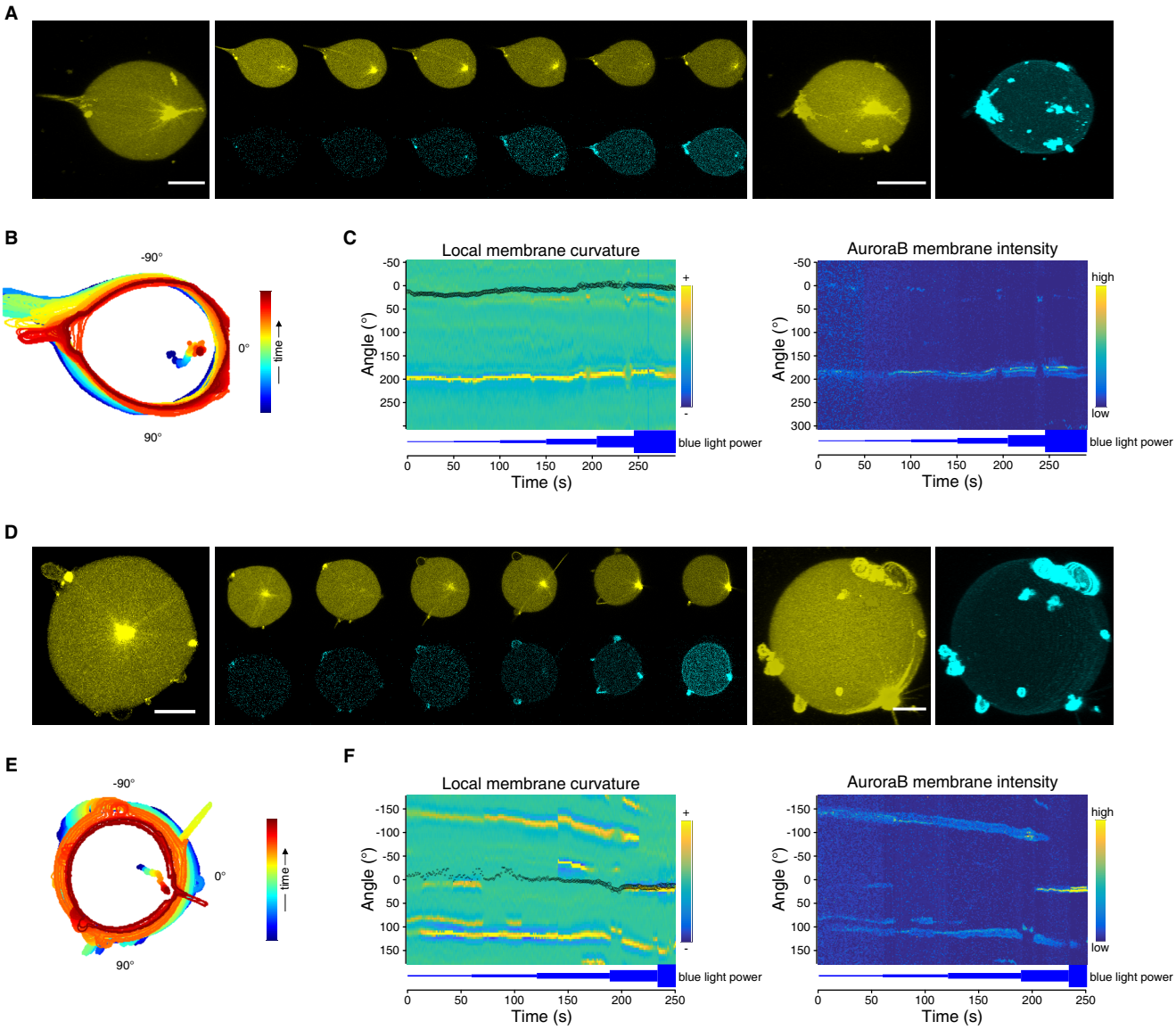

Figure 6. Global light activation stabilizes initial SynMMS morphology

(A) Snapshots of CLSM dose-response of Alexa647-tubulin (yellow) and Alexa488-SspB-AuroraB (cyan) at the equatorial plane of a polar SynMMS during step-wise increase of global illumination with blue light. Maximum intensity projections of Alexa647-tubulin fluorescence of a confocal z-stack obtained before (left) and after (right, together with Alexa488-SspB-AuroraB) the dose-response series are shown. (B) Corresponding GUV contours and (C) kymographs as in Figure 4. Light power increase indicated by thickness of blue line, light power normalized to 1.8 mW/cm². SspB-AuroraB intensity was normalized to the total intensity per frame. (D) Snapshots of CLSM dose-response as above for a star-like SynMMS. (E) Corresponding GUV contours and (F) kymographs. Light power normalized to 1.8 mW/cm². Scale bars are 10 µm.

bioRxiv preprint doi: https://doi.org/10.1101/481887; this version posted June 12, 2019. The copyright holder for this preprint (which was not certified by peer review) is the author/funder. All rights reserved. No reuse allowed without permission.

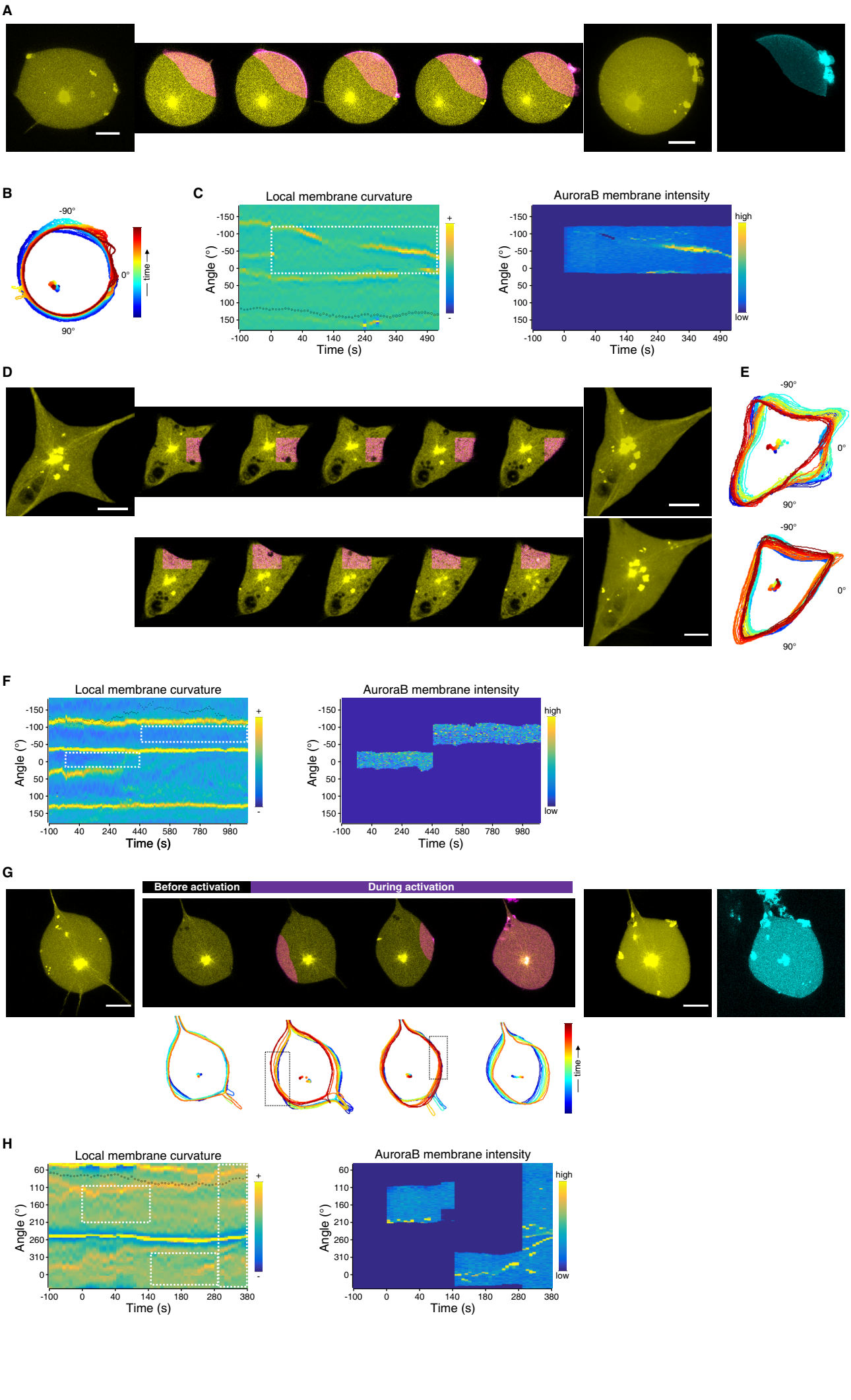

bioRxiv preprint doi: https://doi.org/10.1101/481887; this version posted June 12, 2019. The copyright holder for this preprint (which was not certified by peer review) is the author/funder. All rights reserved. No reuse allowed without permission.

Figure 7. Local stimuli induced morphological transitions depend on initial state
(A) Snapshots of CLSM time lapse of Alexa647-tubulin (yellow) overlaid with Alexa488-SspB-AuroraB (magenta), at the equatorial plane of a star-like SynMMS during continuous local illumination in top right corner (magenta) with blue light. Maximum intensity projections of Alexa647-tubulin fluorescence of a confocal z-stack obtained before (left) and after (right, together with Alexa488-SspB-AuroraB) the time lapse series are shown. (B) Corresponding GUV contours and (C) kymographs as in Figure 4. White dashed rectangle marks activation region and time. (D) Top row: snapshots of CLSM time lapse and maximum intensity projections as above, for a SynMMS with four strong SIC protrusions under local light illumination (magenta). Bottom row: continuation of time lapse with local illumination in another region (magenta). (E) Corresponding GUV contours and (F) kymographs of the combined full time series. (G) Top row: snapshots of CLSM time lapse as above for a star-like SynMMS with a dominant protrusion sequentially activated in different areas (magenta). Bottom row: GUV contours corresponding to above phases of the time lapse. Black rectangles mark activation regions. (H) Corresponding kymographs. Scale bars are 10 µm.

bioRxiv preprint doi: https://doi.org/10.1101/481887; this version posted June 12, 2019. The copyright holder for this preprint (which was not certified by peer review) is the author/funder. All rights reserved. No reuse allowed without permission.

Table 1. Kinetic parameters of stathmin phosphorylation/dephosphorylation and interaction with tubulin, Related to Figure 3

	Stathmin	**Phospho-Stathmin**
Phosphorylation		
k_{cat}/K_m	$11 \pm 0.3 \cdot 10^2$ M^{-1} s^{-1}	
Dephosphorylation		
k_{cat}		0.35 ± 0.03 s^{-1}
K_m		16 ± 3 µM
k_{cat}/K_m		$22 \pm 5 \cdot 10^3$ M^{-1} s^{-1}
Tubulin interaction		
association rate constants	$k_{on1} = 16 \pm 1.6 \cdot 10^5$ M^{-1} s^{-1} $k_{on2} = 9.0 \pm 0.1 \cdot 10^5$ M^{-1} s^{-1}	$k_{on1} = 12.8 \pm 0.7 \cdot 10^3$ M^{-1} s^{-1} $k_{on2} = 17 \pm 1.3 \cdot 10^4$ M^{-1} s^{-1}
dissociation rate constants	$k_{off1} = 0.0480 \pm 0.0007$ s^{-1} $k_{off2} = 1.86 \pm 0.01$ s^{-1}	$k_{off1} = 8 \pm 1$ s^{-1} $k_{off2} = 2.3 \pm 0.1$ s^{-1}
affinities	$K_{D1} = 30 \pm 3$ nM $K_{D2} = 2.00 \pm 0.02$ µM	$K_{D1} = 610 \pm 84$ µM $K_{D2} = 13 \pm 1$ µM

bioRxiv preprint doi: https://doi.org/10.1101/481887; this version posted June 12, 2019. The copyright holder for this preprint (which was not certified by peer review) is the author/funder. All rights reserved. No reuse allowed without permission.

STAR METHODS

KEY RESOURCES TABLE

CONTACT FOR REAGENT AND RESOURCE SHARING

Further information and requests for resources and reagents should be directed to and will be fulfilled by the contact lead, Philippe Bastiaens (philippe.bastiaens@mpi-dortmund.mpg.de).

METHOD DETAILS

Preparation of recombinant proteins

Amino acid sequences of all used constructs are presented in Table S1. All proteins were expressed in *E. coli* BL21 DE3 RIL over night at 18 °C after induction with 0.2 mM IPTG. AuroraB was bicistronically expressed with the INCENP in-box from a modified pGEX6P-2rbs plasmid, which was a gift from A. Musacchio. All other proteins were expressed from a pET24 plasmid as fusions to an N-terminal His_{10}-tag followed by a TEV protease site. 4 – 6 liters of LB medium were used to express stathmin, iLID, and λ-phosphatase (PPλ), whereas 10 – 12 liters of TB medium were used for AuroraB. Cells were lysed by two passes through an Emulsiflex C5 (Avestin, Mannheim, Germany), and the lysate was cleared by 45 – 60 min centrifugation at 20000 rpm in an A27-8x50 rotor (Sorvall/Thermo Fisher Scientific, Dreieich, Germany).

Stathmin and iLID

Gly-stathmin-Cys, Gly-iLID-tRac1, or Gly-C2-iLID were purified via Ni-NTA Superflow (Qiagen, Hilden, Germany) in 50 mM NaP_i pH 8, 300 mM NaCl, 2 mM $MgCl_2$, 0.1 mM β-mercaptoethanol, 10 mM imidazole. The column was washed with 60 mM imidazole, and the protein eluted by a step to 500 mM imidazole. The eluate was supplemented with 2 – 4 mg TEV protease and dialyzed over night against 2 L of 50 mM Tris pH 8, 100 mM NaCl, 1 mM EDTA, 0.1 mM β-mercaptoethanol. The cleaved protein was adjusted to 10 mM imidazole (60 mM for Gly-C2-iLID), and passed again through the Ni-NTA column, followed by gel filtration on a HiLoad 26/600 Superdex 75 pg column (GE Healthcare, Solingen, Germany) in 50 mM Hepes pH 7.5, 200 mM NaCl, 2 mM $MgCl_2$, 2 mM DTT. For iLID constructs, the sample was adjusted to a saturated concentration of flavin mononucleotide prior to gel filtration. Gly-iLID-tRac1 was subsequently geranylgeranylated as described elsewhere (Gavriljuk et al., 2013). We refer to geranylgeranylated iLID as iLID_G.

λ-phosphatase

The protein was purified via cobalt-loaded HiTrap Chelating HP columns (GE Healthcare) in 50 mM NaP_i pH 8, 500 mM NaCl, 2 mM $MgCl_2$, 5 % v/v glycerol, 0.1 mM β-mercaptoethanol, 10 mM imidazole. The washing/elution steps were 60, 200, 500 mM imidazole. The eluted protein was quickly supplemented with 10 mM DTT and digested with TEV protease as above, while dialyzing against 2 L of 50 mM Tris pH 8, 500 mM NaCl, 5 % v/v glycerol, 2 mM $MgCl_2$, 10 mM DTT. The cleaved protein was buffer exchanged back into the sodium phosphate buffer via a HiPrep Desalting 26/10 column (GE Healthcare), adjusted to 10 mM imidazole, and passed again over the chelating column. Finally, the protein was gel filtered on a HiLoad 26/600 Superdex 75 pg column (GE Healthcare) in 50 mM Hepes pH 7.5, 500 mM NaCl, 2 mM $MgCl_2$, 5 mM DTT, 10 % v/v glycerol.

AuroraB

Gly-SspB-AuroraB(45-344)/INCENP(834-902) was purified via Glutathione Sepharose 4 Fast Flow (GE Healthcare) in 50 mM Hepes pH 7.3, 500 mM NaCl, 2 mM $MgCl_2$, 5 mM DTT, 5 % v/v glycerol. The column with bound protein was washed with buffer containing 1 mM ATP, then the protein was eluted with buffer containing 20 mM glutathione and additional DTT up

bioRxiv preprint doi: https://doi.org/10.1101/481887; this version posted June 12, 2019. The copyright holder for this preprint (which was not certified by peer review) is the author/funder. All rights reserved. No reuse allowed without permission.

to 10 mM. The protein was cleaved over night with TEV protease while remaining in the elution buffer. The cleaved protein was buffer exchanged via a HiPrep Desalting 26/10 column (GE Healthcare) to remove glutathione, and passed again through the Glutathione Sepharose column. Gel filtration was carried out on a HiLoad 26/600 Superdex 200 pg column (GE Healthcare) in 50 mM Hepes pH 7.3, 500 mM NaCl, 2 mM $MgCl_2$, 5 mM DTT avoiding concentrating the protein before gel filtration. Finally, the protein was concentrated in an Amicon Stirred Cell (Merck Millipore, Darmstadt, Germany), adjusted to 20% glycerol and hard spun at 400.000 g prior to shock freezing.

Preparation of tubulin and centrosomes

Tubulin purification was performed according to a standard method (Castoldi and Popov, 2003). The following deviations from the published procedure were made: the ratio of buffer/brain mass was 1.5 l/kg, and the Pipes final concentration in the polymerization steps was 333 mM. Purified tubulin was adjusted to a concentration of 200 µM with BRB80 (80 mM Pipes pH 6.8, 1 mM $MgCl_2$, 1 mM EGTA) and stored at –150 °C.

Tubulin was labeled with NHS-Alexa568, -488 or -647 (Thermo Fisher Scientific) or EZ-link NHS-biotin (Thermo Fisher Scientific) according to a standard procedure(Hyman et al., 1991). Typically, 50 mg of tubulin were labeled with a 7.5-fold molar excess of dye assuming 70 % tubulin recovery after the initial polymerization step. Following deviations from the published procedure were made: the dye was added in two steps, each followed by a 15 min incubation, totaling 40 µl DMSO in 1 ml buffer. The reaction was not specifically stopped, and all ultracentrifugation steps were performed at an increased speed of 400.000 g in an MLA-80 rotor (Beckman Coulter, Krefeld, Germany). Labeled tubulin was adjusted to 200 µM with BRB80 and stored at –150 °C.

Centrosomes were isolated from KE37 cells following a standard method (Bornens and Moudjou, 1999).

Protein labeling

Proteins were specifically labeled by sortagging (Popp et al., 2007). The LPETGG peptide was conjugated to NHS-Alexa488, -647, or Atto532 over night at 30 °C (20 mM peptide, 40 mM dye in DMSO, (Thermo Fisher Scientific for Alexa dyes, Atto-tec (Siegen, Germany) for Atto532)) and the reaction was stopped by 100 mM Tris pH 8. Typically, 1 – 3 mg protein (ideally around 300 µM final concentration in the reaction), were mixed with a 4-fold excess of conjugated peptide, ca. 100 µM Sortase A (from *S. aureus*, gift from P. Bieling), and 6 mM $CaCl_2$. For iLID constructs, the sample was additionally adjusted to a saturated concentration of flavin mononucleotide. The reaction was allowed to proceed over night at 18 °C or 4 °C (for PPλ and AuroraB), and the mixture was separated by gel filtration on a Superdex 75 10/300 GL column (GE Healthcare) in appropriate protein gel filtration buffer.

Protein encapsulation in GUVs by cDICE

Encapsulation of proteins in GUVs was achieved by continuous Droplet Interface Crossing Encapsulation (cDICE) following the original method (Abkarian et al., 2011) and relevant parameters are noted below. GUVs without encapsulated components used for experiments performed on the outside were also produced by this method.

0.36 mM lipids were prepared in mineral oil (M3516, Sigma Aldrich/Merck, Darmstadt, Germany). The mixture consisted of eggPC (Sigma Aldrich/Merck) with 15 mol% DOPS and 0.05 mol% DOPE-biotin (both from Avanti Polar Lipids, Alabaster, U.S.A.). Additionally, 0.05 mol% LissamineRhodamineB-DOPE was added for experiments on Alexa488-SspB-AuroraB or Alexa647-SspB-PPλ patterning on GUV membranes. Glass capillaries were typically 10 – 15 µm wide, and pressure was applied using an MFCS-EZ control system (Fluigent, Jena, Germany). cDICE chambers were 3.5 cm wide and were rotated at 1500 – 1800 rpm. 8-well

bioRxiv preprint doi: https://doi.org/10.1101/481887; this version posted June 12, 2019. The copyright holder for this preprint (which was not certified by peer review) is the author/funder. All rights reserved. No reuse allowed without permission.

Lab-Tek chambers (Thermo Fisher Scientific) or 18-well µ-slides (ibidi, Martinsried, Germany) were coated with streptavidin for GUV immobilization.

The base cDICE buffer contained 80 mM Pipes pH 6.8, 75 mM KCl, 2 mM $MgCl_2$, 1 mM EGTA, 1 mM trolox, 0.1 mg/ml β-casein. Additionally, the inner buffer contained 300 mM sucrose and 80 mM glucose, while the outer buffer contained 380 mM glucose. In the hyperosmotic cases, the sucrose concentration inside was lowered by 60 mM and the outside glucose concentration was increased by 160 mM to achieve +100 mOsm or by 180 mM for +120 mOsm (i.e. Figure 1A, F and G, Figures 4, 6, 7). To increase GUV membrane deformability for the experiments depicted in Figure 1C, 50 µl of 1 M glucose was added to 300 µl of the GUVs in solution.

In experiments involving PPλ, EGTA was replaced by 0.8 mM $MnCl_2$. For tubulin polymerization, 2 mM GTP was included, whereas phosphorylation gradient experiments required the presence of soluble tubulin for which 60 µM GTP was included. For SspB-AuroraB activity, 2 mM ATP was added, and in experiments requiring both nucleotides the $MgCl_2$ concentration was increased to 4 mM.

The encapsulation efficiency of tubulin and stathmin was determined by a reference concentration outside of GUVs (Figure S3C), and the used protein concentration for the cDICE preparation was adjusted to yield desired final concentrations, as indicated in respective experiments. For encapsulation of centrosomes, the samples typically contained 10 vol% of a purified centrosome fraction.

For the encapsulation of iLID, SspB-AuroraB, and PPλ, inside concentrations and membrane densities were quantified (Figure S2F) and verified to result in sufficient membrane recruitment and stathmin phosphorylation (see "Imaging and quantification of light-induced protein translocation" and "Measurement and analysis of local stathmin phosphorylation gradients").

Prior to cDICE, the samples were centrifuged for 15 min at 100.000 rpm in a TLA-100 rotor (Beckman Coulter). The centrosomes were never centrifuged, while the tubulin stock was centrifuged separately for 30 min at 60.000 rpm in a RP80-AT2 rotor (Sorvall/Thermo Fisher Scientific).

Imaging of MT asters in GUVs and morphological states

To produce MT asters in GUVs, soluble tubulin and centrosomes were encapsulated as described in "Protein encapsulation in GUVs by cDICE". Stathmin was included as indicated for individual experiments. The following protein concentrations were used in the full reconstituted morphogenic system: 40 or 44 µM (final) tubulin (10 % Alexa647-tubulin), 4 µM (final) stathmin, 5 µM Gly-C2-iLID, 12 µM Alexa488-SspB-AuroraB/INCENP, 1 µM PPλ. Alexa568-tubulin was used for experiments without the signaling system at indicated concentrations.

Microscopic imaging was performed on a Leica SP8 confocal microscope (Leica Microsystems, Wetzlar, Germany) equipped with Leica HyD hybrid detectors, using an HC PL APO 63x/1.2NA motCORR CS2 water objective (Leica Microsystems). The sample was maintained at 33 °C in an environment-control chamber (Life Imaging Services, Basel, Switzerland) Images were acquired after ca. 7 minutes incubation. For temperature induced MT-growth experiments, GUV-containing Lab-Tek chambers were incubated in pre-cooled (4 °C) Stable Z Lab-Tek Stage (Bioptechs, Butler, U.S.A.) for 10 minutes. Then, the stage with the sample was moved onto the microscope and the Stable Z Lab-Tek Stage controller was used to heat the sample to 34 °C, which was reached within 20 minutes, after which images were acquired every minute.

Alexa568 or Alexa488 were excited with a pulsed white light laser source (white light laser Kit WLL2, NKT Photonics, Köln, Germany) at 578 nm (270 – 600 mW/cm²) or 488 nm (220 – 340 mW/cm²), respectively. Detection of fluorescence emission was done in photon

bioRxiv preprint doi: https://doi.org/10.1101/481887; this version posted June 12, 2019. The copyright holder for this preprint (which was not certified by peer review) is the author/funder. All rights reserved. No reuse allowed without permission.

counting mode, restricted with an Acousto-Optical Beam Splitter (AOBS) to 588 – 640 nm or 498 – 540 nm, respectively. Images were taken with 2 or 4 times line averaging at 400 or 200 Hz scanning speed. The pinhole was set to 1 Airy unit in all experiments.

For the experiments performed with the full system (SynMMS), Alexa647 was excited at 650 nm (200 mW/cm² - 700 mW/cm²) at 1000 Hz scanning speed to reduce photodamage. Detection of fluorescence emission was in the range 660 – 750 nm and time-gated by LightGate to minimize signal from laser reflection and background. Activation of iLID and imaging of Alexa488-SspB-AuroraB was done with 488 nm (220 mW/cm²) excitation from a pulsed white light laser source, and fluorescence was detected between 498 – 580 nm. Time lapse images and stacks (1 µm spacing) were taken with 8x line accumulation in line sequential scanning mode. For local activation, 488 nm illumination was restricted to a manually drawn ROI.

Single-filament TIRF-M assay and data analysis

GMPCPP-stabilized microtubule seeds were prepared as follows: 40 µL of 40 µM tubulin mixture (25 % tubulin, 25 % Alexa568-tubulin, 50 % biotinylated tubulin) was polymerized in seed buffer (80 mM Pipes pH 6.8, 1 mM $MgCl_2$, 1 mM EGTA, 1 mM GMPCPP (Jena Bioscience), 5 mM β-mercaptoethanol) at 37 °C. After 30 minutes, 400 µL of prewarmed (37 °C) BRB80 (80 mM Pipes pH 6.8, 1 mM $MgCl_2$, 1 mM EGTA) was added to the tubulin mixture, which was then spun down in a table top centrifuge at 21.000 g for 8 minutes at RT. The microtubule pellet was thoroughly resuspended in 40 µL of BRB80.

TIRF flow chambers were assembled from a biotin-PEG functionalized glass coverslip attached to a PLL-PEG passivated cover slide using double-sided tape (Bieling et al., 2010b). To prevent potential unspecific binding, the flow chamber was first flushed and incubated with 35 µL of blocking buffer (100 β-casein µg/mL, 1 % w/v Pluronic F-127 in assay buffer (40 mM Pipes pH 6.8, 75 mM KCl, 4 mM $MgCl_2$, 0.4 mM EGTA, 1 mM GTP, 100 β-casein µg/mL, 1 mM trolox, 20 mM β-mercaptoethanol). After 5 minutes, the flow chamber was washed two times with 35 µL of assay buffer. Then, the chamber was flushed and incubated with 35 µL of 150 µg/mL Neutravidin (Thermo Fisher Scientific) in assay buffer for another 5 minutes. The flow chamber was washed two times with 35 µL of assay buffer, and then the chamber was flushed and incubated with 35 µL of diluted (1:750) GMPCPP-stabilized microtubule seeds. After 5 minutes, the chamber was washed two times with 35 µL of assay buffer.

After the seeds were immobilized on the surface, 40 µL of protein mixture (10 – 40 µM tubulin (7.5 % Alexa568-labeled), 0 – 20 µM stathmin, 0 – 30 µM phospho-stathmin, 4 µL 10x oxygen-scavenging system (Bieling et al., 2010b), 0. 2% w/v methylcellulose) in assay buffer was introduced into the flow chamber and the two sides were sealed with transparent nail polish.

Imaging was performed at RT with a custom-built TIRF microscope (Olympus IX81 base) with a 60x Olympus APON TIRF objective with TOPTICA IBeam smart 560s laser and a Quad-Notch filter (400-410/488/561/631-640). Temperature was kept at 34 °C by a collar objective heater (Bioptechs). Image acquisition was done with an EM CCD Andor iXon 888 camera controlled by Micromanager 1.4 software. Fiji ImageJ was used for data analysis. For each condition, the average growth velocity and catastrophe frequency were determined from ≥60 microtubules by kymograph analysis.

Determination of MT-aster size in solution

20 µL of protein mixture (10 – 40 µM tubulin (7.5% Alexa568-labeled), 0 – 20 mM stathmin, 0 – 30 µM phospho-stathmin, 2 µl Silica beads (SS06N, Bangs Laboratories, Fishers, U.S.A.), 2 µl 10x oxygen-scavenging system(Bieling et al., 2010b), 0.2 % w/v methylcellulose) was dispersed on a glass cover slide blocked with PLL-PEG(Bieling et al., 2010b) and covered with a glass coverslip pre-coated with PLL-PEG. The edges were sealed with transparent nail polish. Imaging of asters at 33 °C or in temperature ramp experiments were done as described in “Imaging of microtubule asters and morphogenic state transitions in GUVs”. 12 µm thick z-

bioRxiv preprint doi: https://doi.org/10.1101/481887; this version posted June 12, 2019. The copyright holder for this preprint (which was not certified by peer review) is the author/funder. All rights reserved. No reuse allowed without permission.

stacks (1 µm spacing) were taken in the experiments at 33 °C, but single planes were taken during the temperature ramp to maximize the number of imaged fields of view.

For each individual condition, the z-slices at each position were projected in Z by averaging. A mask of the centrosome was made by intensity thresholding and a circle was fitted to determine the center of the centrosome. The projections for all asters where aligned to these centres. The radial intensity profile of the averaged projections (> 30 asters per condition) was extracted with a custom ImageJ macro. Aster size was defined as the distance at 99 % decay, determined by a mono-exponential fit to the radial intensity profile in Origin (OriginLab, Northhampton, U.S.A.).

Morphometric analysis of GUVs

Centrosome Position and Eccentricity

A mask of the GUVs shape was obtained by performing a 2-pixel Mean Filter on the images of fluorescently labeled tubulin at the plane of the centrosome and subsequent thresholding, in ImageJ. An ellipse was fitted to the ROI outline in ImageJ. The centrosome position relative to the center of GUV mask was calculated by:

$$Centrosome\ Position = \frac{\left|\bar{r}_c - \bar{r}_{guv}\right|}{R_{guv}}$$

where $\bar{r}_c = (x_c, y_c)$ and $\bar{r}_{guv} = (x_{guv}, y_{guv})$ are the coordinates of the centrosome and of the geometric center of the fitted ellipse, respectively, and $R_{guv} = (M + m)/4$ where M and m are the major and minor axis of the ellipse. The eccentricity of the fitted ellipse was calculated as:

$$e = \sqrt{1 - \frac{m^2}{M^2}}.$$

3D Morphometric Classification

A 3D mask of the GUV shape was made in the fluorescently labeled tubulin confocal Z-stack, by performing a 2-pixel Mean Filter and thresholding. Masks were imported to MATLAB 2018b. The centrosome position was calculated as above, except that in 3D, $R_{guv} = (PA1 + PA2 + PA3)/6$ where $PA1,2,3$ are the Principal Axis Lengths and $\bar{r}_c$ is the GUV solid mask centroid. These were obtained by applying the in-built function *regionprops3* to the GUV solid mask. To obtain the irregular parameter, the diameter D of the minimal bounding sphere was calculated using the *minboundsphere* function by John D'Errico available at the MathWorks File Exchange. The diameter of the maximal inbound sphere was calculated by taking the maximum of the distance transform of the points contained in the GUV mask, to the GUV surface (edge of the mask) by means of the MATLAB in-built function *bwdist*. The irregular parameter is then obtained as the ratio D/d.

Local curvature kymographs

At each time point of a time-lapse experiments, a mask of the GUV shape was made in the fluorescence image of labeled tubulin (except in Figure 4G and Figure S8, where the mask was done on the labeled SspB-AuroraB image), by performing a 2-pixel Mean Filter and thresholding in ImageJ. A spline was fitted to the Region of Interest (ROI) and then converted into a segmented line format. ROIs and CLSM images were imported to MATLAB 2018b. The points in the segmented line were ordered by their angle with respect to the geometric center of the GUV mask. The curvature was calculated with the function LineCurvature2D written by D. Kroon (University of Twente, August 2011) and available at the MathWorks File Exchange. The curvature at a point was calculated by considering as neighboring left and right points those that were exactly 5 points away from it. The GUV mask at each time of the series was

bioRxiv preprint doi: https://doi.org/10.1101/481887; this version posted June 12, 2019. The copyright holder for this preprint (which was not certified by peer review) is the author/funder. All rights reserved. No reuse allowed without permission.

segmented into 200 angular bins, and the mean curvature at each bin was calculated. The curvature profiles along the membrane and across time therefore formed a matrix of values that was plotted as a kymograph using the MATLAB function *pcolor*.

Fluorescence intensity angular kymographs

For the Alexa488-SspB-AuroraB fluorescence intensity kymographs, the GUV mask at each time point was eroded and dilated using *imerode* and *imdilate* respectively, forming a band following the shape of the GUV. The mask was segmented into 230 angular bins, and the maximum intensity at each bin was taken and plotted in kymographs as above.

Quantification of protein recruitment in protrusions

Local curvature as well as SspB-Aurora fluorescence intensity kymographs were made with equal number and position of segmentation bins, where the masking was in this case performed on the SspB-Aurora fluorescence image. The curvature at each kymograph pixel value was plotted against its corresponding pixel in the fluorescence kymograph.

Imaging and analysis of light-induced SspB-AuroraB translocation

Imaging of blue light-induced translocation of SspB-AuroraB (Alexa488- or Alexa647-labeled) or Alexa647-SspB-PPλ to membrane-bound iLID (Alexa488-labeled or unlabeled) was done on a Leica SP8 confocal microscope (see "Imaging of MT asters in GUVs and morphological states"). iLID was activated by the 458 nm Argon laser line. The following laser powers were used to determine the dose-response properties of the iLID system: near maximal recruitment was observed at 30 mW/cm², so that 65 mW/cm² was used to observe recruitment kinetics and to activate the full morphogenic system. Alexa647 and Alexa488 were excited with 650 and 495 nm white line laser lines, respectively. Detection of fluorescence emission was done in photon counting mode, restricted with an Acousto-Optical Beam Splitter (AOBS) (505 – 560 nm for Alexa488, 660 – 700 nm for Alexa647), and further restricted by LightGate time-gating to minimize signal from laser reflection and background. Images were taken in sequential frame mode when using Alexa647-labeled proteins, where the 488 nm channel would be used to activate iLID and also image it in the cases when iLID was also labeled. For the translocation of Alexa488-labeled SspB-AuroraB, unlabeled iLID was used, and only images of the 488 nm channel were taken to simultaneously activate iLID and image SspB-AuroraB.

For experiments outside of GUVs, varying protein concentrations were added to immobilized GUVs as indicated in individual figure legends. The defined protein concentration in the bulk was used to calculate the protein densities on the membrane using a semi-automated tool in Matlab (MathWorks, Natick, U.S.A.) (Thomas et al., 2015). Bulk depletion effects could be neglected because only 10 – 50 GUVs were present in each 50 µl sample. Binding and unbinding kinetics were fit by exponential functions in Origin (OriginLab).

For experiments inside GUVs, defined starting concentrations are indicated in individual figure legends. To quantify the encapsulation efficiency and membrane densities, a defined protein concentration was added outside of the GUVs as a reference. Analysis was done in the same manner as for the experiments done outside of GUVs.

Local light-induced Alexa488-SspB-auroraB translocation resulted in a lateral gradient along the membrane, which was characterized as follows. A GUV encapsulating Alexa647-SspB-PPλ (SspB) and iLID was imaged for 140 s every 2 s, while irradiating a region of interest encompassing roughly 25% of the membrane for 50s (Figure S2D). The resulting redistribution of SspB along the GUV membrane was fit by 2D CA-simulation (cellular automaton) with the following model: SspB has a minor affinity for the membrane as discernable by the difference in contrast in the images before photo-recruitment with a partitioning resulting from association and dissociation rate constants k_{assoc}/k_{dissoc}; irradiation "creates" a tightly membrane-bound fraction at a rate constant $k_{recruit}$ that is released according to $k_{release}$, but due to the amount of iLID encapsulated concentration of SspB at the membrane is capped at c_{max} (normalized intensity); both membrane-bound iLID and SspB can diffuse laterally (D_{lat}) and SspB in

bioRxiv preprint doi: https://doi.org/10.1101/481887; this version posted June 12, 2019. The copyright holder for this preprint (which was not certified by peer review) is the author/funder. All rights reserved. No reuse allowed without permission.

solution diffuses with a coefficient D_{sol}. The time-lapse of the experiment was normalized to account for bleaching and segmented to improve signal-to-noise. The simulation utilized a time resolution of 0.02 s and matched the pixel size of 0.181x0.181 µm of the confocal micrographs. By varying the parameters of the simulation via function lsqnonlin (Matlab), a best fit was achieved for D_{lat} = 26.4 µm^2/s; $k_{recruit}$ = 4.6/s; $k_{release}$ = 0.016/s; k_{assoc}/k_{dissoc} = 0.38; c_{max} = 4.2 a.u. The time-resolution of the experiment was too slow to resolve the very fast diffusion of SspB in solution, so any D_{sol} > 200 µm^2/s fits the data well. Any discrepancy of kinetic values stems from the fact that the apparent binding and unbinding reaction fit in Figure 2F is a convolution of diffusion, membrane association/dissociation and photo-recruitment kinetics.

Quantifying regularity of SspB-AuroraB clustering on the membrane

To quantify the regularity of SspB-AuroraB spatial distribution on the GUV surface (Figure 2D and Figure S2E) we employed generalized recurrence quantification analysis (Marwan et al., 2007b, 2007a; Mocenni et al., 2010). A recurrence plot (RP) is an advanced technique of nonlinear data analysis that represents a two-dimensional binary diagram indicating the recurrence that occur in an *m*-dimensional phase space within a fixed threshold ε at different times *i,j*. For one-dimensional time series, the RP is expressed as a square matrix of zeros (non-occurrences) and ones (occurrences) of states $\overrightarrow{x_i}$ and $\overrightarrow{x_j}$ of the system: $R_{ij} = \Theta(\epsilon - \|\overrightarrow{x_i} - \overrightarrow{x_j}\|)$, where $\overrightarrow{x_i} \in R^m$, i,j=1,..N, N is the number of measured states $\overrightarrow{x_i}$, $\Theta(\cdot)$ is the step function and $\|\cdot\|$ is a norm. To analyze the regularity of SspB-AuroraB on the surface of the GUV, we used an extension of this analysis for spatial data (Marwan et al., 2007b; Mocenni et al., 2010). For a d-dimensional Cartesian space, $2 \times d$ dimensional spatial recurrence matrix can be defined by: $R_{\vec{i}\vec{j}} = \Theta(\varepsilon - \|\overrightarrow{x_{\vec{i}}} - \overrightarrow{x_{\vec{j}}}\|)$, where $\overrightarrow{x_{\vec{i}}} \in R^m$, $\vec{i}, \vec{j} \in N^d$ (example projections in Figure S2G). The recurrence quantifications are done based on the diagonal hyper-surfaces defined as surfaces of dimension N^d which are parallel to the *hyper-surface of identity* (defined by, $R_{\vec{i}\vec{j}} \equiv 1 \; \forall \; \vec{i} = \vec{j}$). The size of the diagonal hyper-surfaces, l ($\vec{l} = (l, \dots, l)$, $\vec{l} \in N^d$) defined by $(1 - R_{\vec{i}-\vec{1},\vec{j}-\vec{1}})(1 - R_{\vec{i}+\vec{l},\vec{j}+\vec{l}}) \prod_{k_1,\dots,k_d}^{l-1} R_{\vec{i}+\vec{k},\vec{j}+\vec{k}} \equiv 1$, were calculated, and a distribution of surface sizes ($P(l)$) was used to calculate the Information entropy. The Information entropy (ENTR) is defined by $\mathrm{ENTR} = -\sum_{l=l_{min}}^{N} p(l) * \ln(p(l))$, where ln(.) is the natural logarithm, $p(l)$ is the probability of a diagonal hyper-surface with length l, such that $p(l) = {}^{P(l)}/_{N_l}$ and N_l is the total number of diagonal hyper-surfaces with length greater than a fixed minimum length l_{min}.

The 2D maps of the GUV surface were projected from confocal stacks using the Map3-2D software (Sendra et al., 2015). From the spatial map of the SspB-AuroraB on the GUV surface (Figure 2D, Figure S2E), a rectangular region was selected. The regions of SspB-AuroraB aggregation were identified by inspecting the corresponding aggregation in the lipid channel. These regions were masked by thresholding and substituted with NaNs. The horizontal stripes which occasionally appear in the surface maps are result of the projection, and occur when the GUV is large as compared to confocal z-spacing. Since this would artificially increase the regularity as obtained from the RPs, the pixel values in these horizontal stripes (Figure S2E) were replaced with random values drawn from the Poisson distribution corresponding to the noise distribution of the image, that is, defined by the mean intensity of the image. Spatial recurrence quantification analysis with $\varepsilon = 0.3$ and $l_{min} = 3$ was performed on the corresponding rectangular images.

To quantify the SspB-AuroraB fraction in lumen, the 3D z-stack of the GUVs were used. For each stack, the membrane and the lumen were separately masked. The mean intensity per pixel in the 3D lumen (C_{lumen_mean}) and on the 2D membrane ($C_{membrane\_mean}$) were calculated

bioRxiv preprint doi: https://doi.org/10.1101/481887; this version posted June 12, 2019. The copyright holder for this preprint (which was not certified by peer review) is the author/funder. All rights reserved. No reuse allowed without permission.

using imageJ. SspB-AuroraB fraction in the lumen ($C_{lumen/total}$) was calculated using: ($C_{lumen/total} = \frac{C_{lumen\_mean}}{C_{lumen\_mean}+C_{membrane\_mean}}$).

COPY^{o} characterization

Gly-stathmin-Cys was sequentially labeled with two organic dyes to generate the sensor COPY^{o} (^{o} = organic). First, the acceptor dye was conjugated to the C-terminal cysteine. Typically, 3 mg of Gly-stathmin-Cys were incubated with 5 mM TCEP for 1 h at room temperature under an argon atmosphere before buffer exchange via a NAP5 column (GE Healthcare) into degassed 50 mM Hepes pH 7.5, 200 mM NaCl, 2 mM $MgCl_2$. A 10-fold molar excess of Atto655-maleimide (Atto-tec) was added and the mixture incubated for 3 h at room temperature under an argon atmosphere. The reaction was stopped by adding 5 mM DTT. Next, without further purification, the donor dye Atto532 (Atto-tec) was conjugated to the N-terminus as described in the section "Protein labeling". Another sensor version was constructed with Atto647N (Atto-tec) as acceptor dye, which we termed COPY^{o2}.

Initial characterization was carried out by evaluating sensitized emission (Figure S4A). Fluorescence emission spectra were measured with a QuantaMaster fluorescence system (PTI) (exc. 520 nm, em. 530 – 720 nm). 1 µM sensor was in 80 mM Pipes pH 6.8, 75 mM KCl, 1 mM EGTA, 2 mM $MgCl_2$, 20 mM β-mercaptoethanol. 10 µM tubulin was added to measure the decrease of sensitized emission.

Detailed characterization of the FRET properties was done by analysis of donor fluorescence lifetime. Confocal FLIM experiments were performed on a Leica SP8 confocal microscope (see "Imaging of MT asters and morphological states in GUVs") equipped with the FALCON (FAst Lifetime CONtrast) system. Atto532 was excited at 532 nm with a pulse frequency of 40 MHz and emission was collected with three Leica HyD detectors restricted with an Acousto-Optical Beam Splitter (AOBS) to 542 – 563, 568 – 591, and 591 – 620 nm. Data were collected for the donor-only labeled stathmin, free COPY^{o} and COPY^{o2} (3 µM), and tubulin-bound sensors (+ 20 µM tubulin) in cDICE base buffer (see "Protein encapsulation in GUVs by cDICE") + 60 µM GTP, 300 mM sucrose, and additional 1 mM trolox. Photons were collected up to approx. 3000 photons per pixel in the sum of all three detectors. Global analysis of FLIM-FRET was performed with a custom program written in Python following previously describe methods (Grecco et al., 2009, 2010), yielding τ_D (ns) and τ_{DA} (ns). Additionally, all pixel values of the lifetime images were averaged to obtain the absolute lifetimes of the donor for the free and tubulin-bound sensor states (Figure S4B).

Due to the higher signal amplitude obtainable with COPY^{o2}, this variant was used for stopped-flow and most kinetic measurements. However, since Atto647N (acceptor dye in COPY^{o2}) is positively charged and is known to interact with membranes (Hughes et al., 2014), we used COPY^{o} for the measurement of stathmin phosphorylation gradients.

Stopped-flow measurements

Association and dissociation of COPY^{o2} and tubulin were measured in a stopped flow apparatus (Applied Photophysics, Leatherhead, U.K.) with excitation at 535 nm and a 670/30 nm band-pass filter to monitor sensitized emission changes at 25 °C in 80 mM Pipes pH 6.8, 75 mM KCl, 2 mM $MgCl_2$, 20 mM β-mercaptoethanol, 60 µM GTP. COPY^{o2} or phosphorylated COPY^{o2} (P- COPY^{o2}) (see "Time-resolved measurements of AuroraB and λ-PPase activity") was kept constant at 200 nM for the tubulin titration. Dissociation was measured at 200 nM COPY^{o2} and 4 µM tubulin, displacing COPY^{o2} with 60 µM unlabeled stathmin. Data were fit in Origin (OriginLab), and Gaussian error propagation for derived constants was calculated by propagating the errors of the fit.

Determination of enzymatic kinetic parameters

bioRxiv preprint doi: https://doi.org/10.1101/481887; this version posted June 12, 2019. The copyright holder for this preprint (which was not certified by peer review) is the author/funder. All rights reserved. No reuse allowed without permission.

Stathmin phosphorylation and dephosphorylation kinetics were measured using the fluorescence lifetime change or ratiometric signal of COPY^{o} or COPY^{o2} as indicated in the respective figure legends. Lifetime is an absolute, robust and intensity-independent measure of the phosphorylation state and was thereby almost exclusively used for kinetic measurements. Confocal FLIM measurements were performed as described for "Stathmin FRET sensor generation and characterization" with few modifications. Excitation pulse frequency was 20 MHz. Per time-point, 1 – 2 million photons were collected in a 256x256 pixels image. During analysis, 4x spatial binning was applied. Measurements were conducted in cDICE-buffer (see "Protein encapsulation in GUVs by cDICE") + 60 µM GTP, 300 mM sucrose, – EGTA, and additionally 0.8 mM $MnCl_2$ when PPλ was used.

To measure dephosphorylation kinetics, COPY^{o} was pre-phosphorylated (COPY^{o}-P) with 500 nM AuroraB by incubating with 4 mM ATP for 8 h at room temperature and used without further purification. Kinetic traces of dephosphorylation were obtained at varying concentrations of COPY^{o}-P (with tubulin present in at least two-fold excess) and 200 nM PPλ. Values for k_{cat} and K_m were determined from a fit to the Michaelis-Menten equation. Reported errors are errors of the fit, and the error for k_{cat}/K_m was derived by Gaussian error propagation.

Since phosphorylation of stathmin under conditions suitable for Michaelis-Menten analysis was too slow to yield sufficiently stable and analyzable signal amplitudes, we estimated k_{cat}/K_m from monoexponential fits of single-progress curves. 10 µM COPY^{o2} (+ 20 µM tubulin) was phosphorylated by 500 nM or 1 µM SspB-AuroraB, and the data were fit mono-exponentially. The apparent rate constant was converted to a value corresponding to k_{cat}/K_m by taking the used kinase concentrations into account and averaging the two obtained values. Fit errors were propagated by the Gaussian equation.

Note that the derived kinetic parameters for PPλ and SspB-AuroraB do not consider the presence of multiple phosphorylation sites on stathmin or how many of them need to be phosphorylated to induce tubulin dissociation. The parameters apply for the catalysis of the overall transition between free and tubulin-bound stathmin, which is our direct readout and also the relevant state change for the derivation of the signaling gradient.

Measurement of stathmin phosphorylation gradients

Spatial COPY^{o} phosphorylation gradients were imaged and quantified by computing the ratio of Atto655/Atto532 fluorescence emission intensities. First, we derive the relationship between the fluorescence FRET ratio to the fraction of tubulin bound stathmin.

The fluorescence intensity detected at the acceptor channel F_A can be separated into three contributions:

$$F_A = k_A[S] + K_{FA}^{pS}[pS] + K_{FA}^{tS}[tS]$$

where: k_A is a constant proportional to the fluorophore brightness, $[S]$ is the total stathmin concentration, and its product represents the intensity in absence of donor; K_{FA}^{pS} and K_{FA}^{tS} are the contributions to the intensity due to FRET when stathmin is either phosphorylated or tubulin bound, while $[pS]$ and $[tS]$ are their concentrations, respectively. We assume that stathmin can only adopt these two states and hence $[S] = [pS] + [tS]$.

The fluorescence at the donor channel F_D can be written as:

$$F_D = [S]Q = \frac{k_D[S]}{k_D + \alpha K_{FD}^{pS} + (1-\alpha)K_{FD}^{tS}}$$

bioRxiv preprint doi: https://doi.org/10.1101/481887; this version posted June 12, 2019. The copyright holder for this preprint (which was not certified by peer review) is the author/funder. All rights reserved. No reuse allowed without permission.

where Q is the quantum yield, k_D is a constant proportional to the donor fluorophore brightness, and K_{FD}^{pS} , K_{FD}^{tS} are the contributions to donor quenching by FRET, in the corresponding stathmin states, and $\alpha = [pS]/[S]$ is the fraction of tubulin bound stathmin
Normalizing the acceptor fluorescence intensity to the total stathmin concentration yields:

$$F_A = \left[k_A + K_{FA}^{pS}\alpha + K_{FA}^{tS}(1-\alpha)\right][S]$$

After rearranging terms, we obtain:

$$F_A = \left[(k_A + K_{FA}^{tS}) + \alpha(K_{FA}^{pS} - K_{FA}^{tS})\right][S]$$

Taking the FRET fluorescence ratio of acceptor fluorescence to donor fluorescence can be then expressed as:

$$R = \frac{F_A}{F_D} = \frac{1}{k_D}\left[(k_A + K_{FA}^{tS}) + \alpha(K_{FA}^{pS} - K_{FA}^{tS})\right]\left[k_D + \alpha K_{FD}^{pS} + (1-\alpha)K_{FD}^{tS}\right]$$

where $R = F_A/F_D$ is the fluorescence FRET ratio. Rearranging:

$$R = \frac{F_A}{F_D} = \frac{1}{k_D}\left[(k_A + K_{FA}^{tS}) + \alpha(K_{FA}^{pS} - K_{FA}^{tS})\right]\left[(k_D + K_{FD}^{tS}) + \alpha(K_{FD}^{pS} - K_{FD}^{tS})\right]$$

Grouping the remaining constants between parenthesis as,
$K_1 = k_A + K_{FA}^{tS}$, $K_2 = K_{FA}^{pS} - K_{FA}^{tS}$, $K_3 = k_D + K_{FD}^{tS}$, $K_4 = K_{FD}^{pS} - K_{FD}^{tS}$

Simplifies the expression to:

$$R = \frac{1}{k_D}[K_1 + \alpha K_2][K_3 + \alpha K_4]$$

Distributing the product yields:

$$R = \frac{1}{k_D}[K_1K_3 + \alpha(K_1K_4 + K_2K_3) - \alpha^2K_2K_4]$$

Since FRET is negligible in the tubulin bound state, K_{FA}^{tS} and K_{FD}^{tS} are negligible, and because the FRET efficiency of COPY^o is < 30 %, the product $K_{FD}^{pS}K_{FA}^{pS}$ is also negligible since both magnitudes depend on the intrinsic FRET efficiency. Hence, the quadratic term becomes negligible, so we can solve for α as:

$$\alpha = \frac{k_DR - K_1K_3}{K_1K_4 + K_2K_3}$$

Therefore, the fraction of phospho-stathmin α is an approximate linear function of the fluorescence FRET ratio R.

Measuring FRET by ratiometric intensity measurements results in higher signal to noise, than fluorescence lifetime measurements and therefore provides the sensitivity to detect spatial gradients. Confocal imaging was done on a Leica SP8 microscope (see "Imaging of microtubule asters and morphogenic state transitions in GUVs"). COPY^o was excited at 532 nm, and

bioRxiv preprint doi: https://doi.org/10.1101/481887; this version posted June 12, 2019. The copyright holder for this preprint (which was not certified by peer review) is the author/funder. All rights reserved. No reuse allowed without permission.

detection was done in photon counting mode, restricted to 542 – 560 nm and 640 – 750 nm for donor and acceptor, respectively. The imaging focus was maintained by Leica Adaptive Focus Control. Imaging conditions were identical when measuring outside of or inside GUVs. The following protein concentrations were used for encapsulation: 40 µM (final) tubulin, 4 µM (final) COPY°, 5 µM C2-iLID, 12 µM SspB-AuroraB (unlabeled), 1 µM PPλ. Outside GUVs the following concentrations were used: 20 µM tubulin, 10 µM COPY°, 1 µM iLID_G, 1.5 µM SspB-AuroraB (unlabeled), and varying PPλ concentrations as indicated.

For the "dark" state (no blue-light photoactivation and hence no SspB-AuroraB translocation) 40 images at the equatorial plane were taken with 3 s intervals. This spacing was necessary to prevent unwanted iLID activation by 532 nm light. Inside GUVs, this illumination still led to substantial iLID activation, so that no gradient images for the state in the absence of photo-activating blue light were obtained.

Activation of iLID was done with the 458 nm Argon laser line for the duration of 3 min with 3 s intervals. iLID Flavin autofluorescence was detected between 568 – 520 nm to be used as a membrane marker during the analysis.

For the activated state, 40 images were taken with minimal intervals. A sequential line scan was performed between iLID activation and COPY° imaging.

In case there was any GUV movement during image series acquisition, the frames were aligned in ImageJ using the MultiStackReg plugin based on StackReg (Thévenaz et al., 1998). Then, all images of the series were added (more precise than averaging, and made possible by photon counting). We observed an optical xy-aberration between the donor and acceptor channels, which led to asymmetric edge effects around the GUVs in the ratio image. To avoid these, the channels were manually registered to yield a symmetric ratio image calculated as acceptor/donor. Radial profiles were extracted from the ratio images by a custom macro in ImageJ using iLID autofluorescence as a marker to determine the starting position at the membrane and align the profiles of individual GUVs.

To visualize the pStathmin gradient, we measured 7 – 8 µm thick z-stacks of the ratio (1 µm spacing, 10 images per slice) around the equatorial plane of a GUV. From these stacks, maximum intensity projections along the z-axis were calculated.

Paradigmatic model of morphogenesis

The behavior of the two sub-systems, the self-organized morphogenesis of the encapsulated MT-aster as well as the spatial organization of SspB-AuroraB clusters on the GUV membrane, when isolated, can be conceptualized with paradigmatic reaction-diffusion models, where self-amplification of local structures triggers depletion of its free substrate. Generically, this can be represented as:

$$\frac{\partial u_i}{\partial t} = f(u_i, v_i) + D_{u_i}\frac{\partial^2 u_i}{\partial x^2}$$
$$\frac{\partial v_i}{\partial t} = -f(u_i, v_i) + D_{v_i}\frac{\partial^2 v_i}{\partial x^2} \qquad \text{(Eqs.1)}$$

where $u_i + v_i = c_i = const., i = 1,2$, and u_1 corresponds to the self-amplified MT-bundles that generate membrane protrusions (Figure 1D) and u_2 to the SspB-AuroraB clusters on the membrane (Figures 2F), whereas $v_{1,}$ represents the astral MTs and v_2- protein monomers. In SynMMS, a joint dynamical system is established, where the protrusion-induced change in the membrane geometry enhances SspB-AuroraB translocation and thereby its activity, that in turn locally promotes the MT-growth (Figure 5B). The joint system is thus described with:

$$\frac{\partial u_1}{\partial t} = g\left(u_1, v_{1,} u_2\right) + D_{u_1}\frac{\partial^2 u_1}{\partial x^2}$$

bioRxiv preprint doi: https://doi.org/10.1101/481887; this version posted June 12, 2019. The copyright holder for this preprint (which was not certified by peer review) is the author/funder. All rights reserved. No reuse allowed without permission.

(Eqs.2)

$$\frac{\partial v_1}{\partial t} = -g(u_1, v_{1,} u_2) + D_{v_1}\frac{\partial^2 v_1}{\partial x^2}$$

$$\frac{\partial u_2}{\partial t} = g(u_2, v_{2,} u_1) + D_{u_2}\frac{\partial^2 u_2}{\partial x^2}$$

$$\frac{\partial v_2}{\partial t} = -g(u_2, v_{2,} u_1) + D_{v_2}\frac{\partial^2 v_2}{\partial x^2}$$

To investigate the dynamical possibilities of this system, we applied Linear Perturbation Analysis (LPA) (Grieneisen, 2009; Marée et al., 2006) that in turn allows to analyze the bifurcation structure of a reaction-diffusion (RD) system. In brief, the method takes advantage of the diffusion discrepancy $D_{u_i} \ll D_{v_i}$ and considering the limit $D_{u_i} \to 0, D_{v_i} \to \infty$, the stability of the homogenous steady state can be probed with respect to a 'local' perturbation in the form of a narrow peak of u_i with a negligible total mass, at some location in the domain. In this limit, the localized peak of u_i ($u_{L,i}$) does not influence the surrounding background u_i levels ($u_{G,i}$), whereas due to the 'infinitely fast' diffusion, v_i can be described by a single global variable ($v_{G,i}$) that is approximately uniformly distributed in space. This allows writing a set of ODEs that describe the evolution of the perturbation peak as:

(Eqs.3)

$$\frac{du_{L,1}}{dt} = g(u_{L,1}, u_{L,2}, c_1 - u_{G,1})$$

$$\frac{du_{G,1}}{dt} = g(u_{G,1}, u_{G,2}, c_1 - u_{G,1})$$

$$\frac{du_{L,2}}{dt} = g(u_{L,2}, u_{L,1}, c_2 - u_{G,2})$$

$$\frac{du_{G,2}}{dt} = g(u_{G,2}, u_{G,1}, c_2 - u_{G,2})$$

Dynamics of this ODE system (Eqs.3) under variation of the total SspB-AuroraB concentration (c_2) was explored using the Xppaut bifurcation software to produce Figure 5C,

$$g(u_{L,1}, u_{L,2}, c_1 - u_{G,1}) = (k_0 + k_3 \cdot u_{L,2} + \gamma_1 \cdot {u_{L,1}}^2) \cdot (c_1 - u_{G,1}) - \omega_1 \cdot u_{L,1}$$

$$g(u_{G,1}, u_{G,2}, c_1 - u_{G,1}) = (k_0 + k_3 \cdot u_{G,2} + \gamma_1 \cdot {u_{G,1}}^2) \cdot (c_1 - u_{G,1}) - \omega_1 \cdot u_{G,1}$$

$$g(u_{L,2}, u_{L,1}, c_2 - u_{G,2}) = (k_0 + k_4 \cdot u_{L,1} + \gamma_2 \cdot {u_{L,2}}^2) \cdot (c_2 - u_{G,2}) - \omega_2 \cdot u_{L,2}$$

$$g(u_{G,2}, u_{G,1}, c_2 - u_{G,2}) = (k_0 + k_4 \cdot u_{G,1} + \gamma_2 \cdot {u_{G,2}}^2) \cdot (c_2 - u_{G,2}) - \omega_2 \cdot u_{G,2}$$

with $k_0 = 0.067, k_3 = 1, k_4 = 0.5, \gamma_1 = 0.4,\ \gamma_2 = 5, \omega_1 = 0.5, w_2 = 5$. The insets in Figure 5C correspond to reaction-diffusions simulations of (Eqs. 2) with different total SspB-AuroraB. From left to right: c_2=800, 1500, 2750 respectively and c_1=1000 in all cases.

For the reaction-diffusion simulations (Figures 5D – 5G and Figure S6F), an external signal source corresponding to global light illumination is applied that increases the amount of free AuroraB monomers on the membrane and thereby enhances the cooperative clustering. This is

bioRxiv preprint doi: https://doi.org/10.1101/481887; this version posted June 12, 2019. The copyright holder for this preprint (which was not certified by peer review) is the author/funder. All rights reserved. No reuse allowed without permission.

implemented by including ρ which is proportional to the signal strength as $\rho \cdot \gamma_2 \cdot u_2{}^2$. To model the influence of local signal, a Gaussian distribution was used.

For Figures 5D – 5G all parameters are kept the same, except: for Figure 5D, c_2 = (2750, 1500); for Figure 5E, c_2 = 2750; for Figure 5F, c_2 = 5750, c_1=2000, $\gamma_1 = 1,\ \gamma_2 = 0.5$; and for Figure 5G c_2 = 2750, c_1 = 2000. For Figures S6F left, c_2 = 2750 and right, c_2 = 2750, $\gamma_1 = 1,\ \gamma_2 = 0.5$. The RD simulations were performed in 1D using a custom-made Python code, with $D_{u,i} = 0.1, D_{v,i} = 40$. The integration time was set to $1.5 \cdot 10^8$, the time step – $7.5 \cdot 10^{-5}$, for a total of 10^3 spatial bins with step size 0.1, and periodic boundary conditions.

Reaction-diffusion simulation of gradients

We utilize numeric simulations of the reaction diffusion system to visualize the gradients resulting from localizing a kinase to the membrane of a GUV. Our kinetic measurements confirm two tubulin binding sites on stathmin. As the low affinity site (K_D = 2 µM for the unphosphorylated, > 200 µM for the phosphorylated state) has a high turnover rate, we consider a simplified setup of five "species": 1) free tubulin dimers and 2) free stathmin, 3) stathmin tubulin complex (in a 1:1 stoichiometry), 4) phosphorylated stathmin tubulin complex and 5) phosphorylated free stathmin. Here, species 2-5) are actually weakly associated with a second tubulin dimer that slows down effective diffusion, but whose binding state is not strongly influenced by phosphorylation. We assume that the pairwise association/dissociation and kinase/phosphatase reaction can be considered first-order processes governed by a back and a forth rate constant (equivalent to sub-saturation Michaelis-Menten-Kinetics) to reduce the number of parameters in the system. Considering a well-mixed volume (diffusion much faster than reaction), the balance of kinase/phosphatase reaction determines the steady-state levels of phosphorylated stathmin. For our measurements of k_{cat}/k_M (PPase 0.02 $\mu M^{-1}\ s^{-1}$; kinase 0.0011 $\mu M^{-1}\ s^{-1}$), at a stoichiometry of 1:1 about 5-10% of stathmin should be phosphorylated with a homogenously flat distribution in the GUV. By recruitment to the membrane, the concentration of the kinase is increased by a factor of up to 500. For this, a 5x increase of fluorescence intensity suffices, as the resolution of ~500 nm dilutes the signal of the "shell" of recruited kinase with a thickness of ~5 nm close to the membrane. Such recruitment leaves a significant fraction of kinase in solution, but due to the unchanged phosphatase activity resulting in a lowered phosphorylated fraction. In a see-saw-like manner, the high kinase activity at the membrane "inverts" phosphorylation after recruitment and leave a fraction of <4% *un*phosphorylated stathmin there. If the phosphatase activity was also recruited, but to the center of the GUV, the result would be a linear gradient completely independent of diffusion, the amplitude of which would solely be determined by the relative strength of kinase and phosphatase activity. In such a case, diffusion would only change the amount of phosphorylated protein transported and how fast the gradient is established. However, as the soluble phosphatase is distributed evenly, the shape of the gradient arises from the interplay of diffusion, phosphatase activity and association/dissociation kinetics of stathmin-tubulin. This defeats any attempt of analytical solutions in more than simplified geometries and requires solving the underlying differential equations numerically.

To this effect, reaction-diffusion simulations are performed by cellular automata approach (Schmick et al., 2014) 1D, with a resolution of 0.01 µm per space unit. This corresponds to the kinase homogenously localized to the membrane of a spherical GUV. For a diffusion coefficient of 20 $\mu m^2\ s^{-1}$ of species 3+4), this translates to a diffusant radius of 3 space units and a time resolution of the simulation of 0.01 s per time step. The diffusant radius of species (1+2+5) is set to 4 space units (corresponding to a slightly too high D = 35 $\mu m^2\ s^{-1}$, avoiding numerical inconsistencies). Initial conditions were set for all association/dissociation of all species in steady-state without any kinase activity and setting kinase activity to its maximum instantaneously at t_0. Simulations continue until the relative change of the vectorial sum of all

bioRxiv preprint doi: https://doi.org/10.1101/481887; this version posted June 12, 2019. The copyright holder for this preprint (which was not certified by peer review) is the author/funder. All rights reserved. No reuse allowed without permission.

concentrations $<10^{-9}$ results in a steady-state distribution of all species. For dissociation/association reactions, the relevant rate constants are: $k_{on,stath} = 16\ s^{-1}$, $k_{off,stath} = 0.048\ s^{-1}$, $k_{on,p\text{-}stath} = 1.8\ s^{-1}$, $k_{off,p\text{-}stath} = 2.3\ s^{-1}$ and remain fixed across all simulations. In most experimental conditions, 2 – 5 µM of soluble kinase are used with a corresponding activity of $k_{kin} = 0.004\ s^{-1}$. We estimate the increase of concentration after translocation to the membrane by a factor of 200 – 500 to yield a kinase activity of $k_{kin} = 1\ s^{-1}$ for a depletion of 50% soluble kinase. Conversely, the phosphatase activity at 1 µM can be estimated as $k_{PP\lambda} = 0.02\ s^{-1}$. These parameters produce a spatial distribution of the species (1-5) depicted in Figure S4F (left panel). Higher diffusivity of phospho-stathmin as compared to the tubulin-stathmin-complex (molecular weight 220 kDa, $D = 20\ \mu m^2\ s^{-1}$) leads to a depletion of the total stathmin (free, phosphorylated and tubulin-bound, cyan line in Figure S4F (left panel) at the membrane. This distribution is mirrored by the total tubulin due to its high association rate to stathmin.

Gradients of phosphorylated stathmin and free tubulin result from the competition of kinase activity that effectively "deposits" tubulin near the membrane and entropic redistribution by diffusion as well as rebinding to dephosphorylated unbound stathmin as driven by dephosphorylation. An activity of lambda phosphatase of $0.02\ s^{-1}$ is sufficient to let the gradients decline within 1.5 µm distance from the membrane even at 10000 times faster kinase activity. Interestingly, varying the phosphatase activity for a kinase activity of $1\ s^{-1}$ in agreement with our measurements shows an optimally steep gradient for 100 times slower phosphatase activity. Low phosphatase activity can saturate the GUV with phospho-stathmin and therefore free tubulin due to the shift in partitioning and yields a flat gradient with a high off-set. The highest phosphatase activity abolishes the phospho-stathmin gradient (zero amplitude and offset). Due to the association rate to (phospho-)stathmin being about 20 times faster than even kinase activity, the gradient of free tubulin is "locked" to the phospho-stathmin gradient (Figure S4E).

We additionally perform simulations in 2D to assess the impact of local geometry of protrusions on the gradients of free tubulin. Protrusions feature a much higher surface-to-enclosed-volume ratio compared to undeformed spherical GUVs. Assuming a homogeneous distribution of kinase activity per μm^2 of surface, we plot the gradient of free tubulin in a GUV with a radius of 32 µm, featuring protrusions of 250 nm diameter with varying lengths (0.5 µm – 22.5 µm). The kinetic parameters were kept identical to previous 1D simulation, specifically with the activities of phosphatase ($0.02\ s^{-1}$) and kinase ($0.004\ s^{-1}$ homogenously in the medium and $1\ s^{-1}$ homogenously at membrane).

DATA AND SOFTWARE AVAILABILITY

All custom-made code is available upon request to the corresponding author.

bioRxiv preprint doi: https://doi.org/10.1101/481887; this version posted June 12, 2019. The copyright holder for this preprint (which was not certified by peer review) is the author/funder. All rights reserved. No reuse allowed without permission.

Video S1. Time-lapse of temperature-induced morphological state transitions corresponding to Figures 1D, S1E and S1F (from left to right).

Video S2. Time-lapse of temperature-induced morphological state transitions corresponding to Figures 1F and 1G (from left to right). Top: Alexa647- or Alexa488-tubulin fluorescence, bottom: corresponding GUV contour plots.

Video S3. Time-lapse of light-induced MT-aster growth in SynMMS corresponding to Figure 3J (yellow: Alexa647-tubulin, magenta: Alexa488-SspB-AuroraB).

Video S4. Time-lapse of Alexa647-tubulin (yellow) and Alexa488-SspB-AuroraB (cyan) at the equatorial plane of spherical SynMMS (top row) and SynMPS (right) corresponding to Figure 3D. Corresponding GUV contour plots on the right.

Video S5. Left: time-lapse of Alexa647-tubulin (yellow) and Alexa488-SspB-AuroraB (magenta) at the equatorial plane of SynMMS corresponding to Figure 4I. Right: corresponding GUV contour plot.

Video S6. Time-lapse of Alexa647-tubulin (yellow) and Alexa488-SspB-AuroraB (cyan) at the equatorial plane of a polar SynMMS (top row) and a star-like SynMMS (bottom row) corresponding to Figures 6A and 6D. Corresponding GUV contour plots on the right.

Video S7. Top: time-lapse of Alexa647-tubulin (yellow) and Alexa488-SspB-AuroraB (magenta) at the equatorial planes of star-like SynMMS corresponding to Figures 7A, 7D and 7G (from left to right). Bottom: corresponding GUV contour plots.